Earth System
Open Access
Science
Data
Discussions

Mapping 10-m global impervious surface area (GISA-10m) using multi-source geospatial data

Xin Huang[1,2], Jie Yang[1], Wenrui Wang[1], Zhengrong Liu[1]

[1] School of Remote Sensing and Information Engineering, Wuhan University, Wuhan, 430079, P.R. China
[2] State Key Laboratory of Information Engineering in Surveying, Mapping and Remote Sensing, Wuhan University, Wuhan, 430079, P.R. China

Correspondence to: Jie Yang (yang9tn@163.com)

Abstract. Artificial impervious surface area (ISA) documents human footprints. Accurate, timely, and detailed ISA datasets are therefore essential for global climate change and urban planning. However, due to the lack of sufficient training samples and operational mapping methods, global ISA mapping at 10-m resolution is still lacking. To this end, we proposed a global ISA mapping method leveraging multi-source geospatial data. Based on the existing satellite-derived ISA maps and the crowdsourcing OpenStreetMap (OSM), 58 million training samples were extracted via a series of temporal, spatial, spectral, and geometric rules. Combined with over 2.7 million Sentinel optical and radar images on the Google Earth Engine, we produced the 10 m global ISA dataset (GISA-10m). Based on the test samples that are independent to the training set, GISA-10m embraced an overall accuracy greater than 86%. In addition, the GISA-10m was comprehensively compared with the existing global ISA datasets, and the superiority of GISA-10m was demonstrated. It was found that China and the United States embraced the largest ISA and road area. The global rural ISA was 2.2 times that of urban while rural road area was 1.5 times larger than that of urban region. The global road area accounted for 14.2% of the global ISA, 57.9% of which was located in the top ten countries. Generally, the produced GISA-10m dataset and the proposed sampling and mapping method are able to achieve rapid and efficient global mapping, and have potential for detecting other land covers. It was also indicated that global ISA mapping can be improved by incorporating refined OSM data. GISA-10m can be used as a fundamental parameter for Earth system science, and provide valuable support for of urban planning and water cycle study. The GSIA-10m can be freely downloaded from http://doi.org/10.5281/zenodo.5791855 (Huang et al, 2021).

1 Introduction

The land dominated by humans has expanded rapidly over the past decades (Friedl et al., 2010; Goldewijk, 2001), resulting in a large amount of terrestrial surface covered by impervious surface area (ISA) (Gong et al., 2020a). ISA is mainly composed of artificial materials, such as gravel, glass, asphalt, and metals (Tian et al., 2018). ISA prevents or decelerates water infiltration while blocks evapotranspiration, which affects the terrestrial water cycle and thermal environment (Qin et al., 2018; Yang et al., 2019). With more attention attracted to the impact of urban sprawl on the global climate environment (United Nations, 2016, 2018), the global monitoring of ISA would depict the anthropic implications on the water cycle, land

cover, biodiversity (Leng et al., 2015; Li et al., 2020a; Qin et al., 2017). In addition, ISA morphology is also an important parameter for urban planning, socio-economics and population studies (Voss, 2007). In summary, accurate and timely monitoring of global ISA dynamics is valuable for urban habitability (Herold et al., 2006), sustainable development (Dewan and Yamaguchi, 2009), and terrestrial ecosystem services (Goetz et al., 2003).

35   The global ISA monitoring via satellite remote sensing data has long been recognized. Early efforts usually focused on global ISA mapping using coarse-resolution data, e.g., DMSP (Defense Meteorological Satellite Program) and MODIS (Moderate Resolution Imaging Spectroradiometer) data (Friedl et al., 2010; Huang et al., 2021b; Small et al., 2005). With the free availability of Landsat data and advances in geospatial cloud platforms (e.g. Google Earth Engine, GEE), recent studies have focused on global annual ISA mapping at 30 m (Gong et al., 2020b; Gorelick et al., 2017; Liu et al., 2020b; Woodcock

40   et al., 2008). For instance, Huang et al., (2021b) generated the global annual ISA dataset GISA (Global Impervious Surface Area) from 1972 to 2019 using over three million Landsat data. Although efforts have been paid to the global ISA monitoring, few studies focused on global ISA mapping at 10-m resolution. Recently, Corbane et al., (2021) generated the Global Human Settlement Layer (GHSL2018) using Sentinel-2 composites and convolutional neural networks. However, GHSL2018 focused more on human settlements and lacks depiction of ISA such as transportation facilities. In addition to

45   these thematic datasets, ISA was also documented in land cover products. For example, Gong et al., (2019) obtained a land cover map FROM_GLC10 (10-m Finer Resolution Observation and Monitoring of Global Land Cover) for 2017 using Sentinel-2 images. However, the accuracy of ISA in the land cover datasets may not sufficient to meet the needs of global climate change studies and urban planning (Gong et al., 2020b). Therefore, the 10 m global ISA thematic datasets are in urgent need to support various fine-scale applications.

50   Synthetic Aperture Radar (SAR) performs well in the case of ISA mapping due to its clear response to high-rise buildings and ability to penetrate clouds (e.g. Sentinel 1) (Zhang et al., 2014). SAR data is potential for reducing the common false alarms derived from the optical images, such as bare soil, but it can be affected by complex terrain and shadows. Therefore, existing literatures have invested the collaboration of radar and optical data to improve ISA mapping. For example, Zhang et al., (2020) combined Landsat-8 and Sentinel-1 data to produce a 30 m global ISA dataset (Global Land Cover Fine

55   Classification System, GLCFCS). Similarly, Marconcini et al., (2020) used Landsat-8 and Sentinel-1 data to outline the world settlement footprint (World Settlement Footprint, WSF) based on support vector machine classifier. Although the current studies have demonstrated the effectiveness of combining multi-source (e.g. radar and optical) remote sensing data for ISA mapping, they usually focus on regional or national scales (Ji et al., 2020; Lin et al., 2020). In addition, combining data with different resolutions for ISA mapping may increase the uncertainty of results. In particular, both Zhang et al.,

60   (2020) and Marconcini et al., (2020) generated global ISA (or settlement) datasets by using Landsat-8 and Sentinel-1 data, but their resolutions were different, 30 m and 10 m, respectively (Table 1). Generally, 10-m global ISA mapping based on the multi-source remote sensing data (e.g. Sentinel-1 and 2) have been insufficiently investigated in the current literature (Table 1).

65 **Table 1. The existing global ISA datasets.**

Name and abbreviation	Data and time span	Nominal resolution	Source of training sample	Classification method and strategy	Type Definition
Global Impervious Surface Area 30 m, *GISA* (Huang et al., 2021a)	Landsat; 1972—2019	30 m	MODIS land cover, Climate Change Initiative land cover, GHSL, FROM_GLC	Random forest classifiers via hexagonal partition	Artificial impervious surface
Global Artificial Impervious Area, *GAIA* (Gong et al., 2020b)	Landsat; 1985—2018	30 m	Visual interpretation	An exclusion-Inclusion approach via 3.5° grid	Artificial impervious area
Global Annual Urban Dynamics, *GAUD* (Liu et al., 2020b)	Landsat; 1985—2015	30 m	GAIA, GHSL, Global Urban Land, Global Urban Footprint	Random forest classifiers via 1° grid; temporal segmentation	Urban extent
Global Human Settlement Layer, *GHSL2018* (Corbane et al., 2021)	Sentinel-2; 2018	10 m	Microsoft building footprint, Facebook settlement, European settlement map, GHSL	Convolutional neural network models within Universal Transverse Mercator zones	Human settlement
Finer Resolution Observation and Monitoring of Global Land Cover, *FROM_GLC 10* (Gong et al., 2019)	Sentinel-2; 2017	10 m	Visual interpretation	Random forest classifiers	Impervious surface
World Settlement Footprint, *WSF2015* (Marconcini et al., 2020)	Landsat-8, Sentinel-1; 2015	10 m	Thresholding for spectral index, radar and slope data	SVM classifiers via 1° grid	Human settlement
Global Land Cover with Fine Classification System, *GLCFCS* (Zhang et al., 2020a)	Landsat-8, Sentinel-1; 2015	30 m	GlobeLand30	Random forest classifiers via 5° grid	Impervious surface
Global Impervious Surface Area 10 m, *GISA-10m* (this study)	Sentinel-1, Sentinel-2; 2016	10 m	GISA, OSM GlobeLand30, FROM_GLC10	Random forest classifiers via hexagonal partition	Artificial impervious surface

From the perspective of global ISA mapping method, supervised classification has been widely employed (Table 1). The quality of training samples is the major factor affecting the classification results (Foody, 2009). Visual interpretation and automatic extraction from existing datasets are two common methods to generate training samples. Visually-interpreted samples are usually accurate but labour-intensive. Therefore, it is often used for classifications at regional scale (Yang et al.,

70 2020). On the other hand, samples generated from existing datasets have been proved to be efficient for global ISA mapping in recent years (Marconcini et al., 2020; Zhang et al., 2020a). In fact, ISA samples are diverse, as their response to different sensors varies with materials, geometry, atmospheric conditions, and viewing angles. Therefore, accurate and sufficient samples are required to address the above issue for the purpose of consistent ISA mapping at the global scale. Given the higher spatial resolution (10 m) of the Sentinel satellites, it remains challenging to obtain high-quality and adequate training

75 samples for 10-m global ISA mapping.

In general, due to the difficulty of collecting training samples and the limitation of computational and storage capacity to deal with the massive data, efficient methods and accurate datasets regarding 10 m global ISA mapping are lacking. Therefore, in this study, we proposed a global ISA mapping method that leverages multi-source geospatial data to mapping 10-m global impervious surface area (GISA-10m). To our knowledge, this was the first global 10 m ISA mapping based on

80 Sentienl-1 and 2 data. Specifically, combining the multi-source remote sensing and the crowdsourcing OpenStreetMap data, we proposed a sample generation method involving a series of temporal, spatial, spectral, and geometric rules to collect training samples with global coverage. Besides, an adaptive hexagonal partition strategy was used for multi-source feature extraction and classification. Finally, the accuracy of GISA-10m was assessed by three independent sample sets. Meanwhile, we compared the GISA-10m with existing datasets to better reflect its quality, and the ISA distribution in the global urban

85 and rural regions was analysed. Ablation experiments were further conducted to demonstrate the feasibility of OSM data in global ISA mapping.

2 Data

2.1 Remote sensing data

Sentinel-2 optical and Sentinel-1 SAR data were used in the GISA-10m mapping. Sentinel-2 is a high-resolution

90 multispectral imaging mission by European Space Agency (ESA) Copernicus program. The first Sentinel-2 satellite (Sentinel-2A) has been acquiring high-resolution Earth observation data since June 2015, consisting mainly of four 10-m resolution visible and near-infrared bands, six 20-m resolution red-edge and shortwave infrared bands, and three 60-m bands (Drusch et al., 2012; Zhang et al., 2018). After tested and adjusted, complete global coverage was obtained for Sentinel-2 satellite in 2016 (Fig. S2). Therefore, we used all available Level-1C top of atmosphere (TOA) reflectance data acquired in

95 2016 for our 10-m ISA mapping. The systematic radiometric calibration, geometric and terrain correction have been performed for the Level-1C TOA data by the ESA. Clouds and shadows were removed via the quality band to obtain cloud-free pixels.

Sentinel-1A was launched on April 2014, carrying a C-band synthetic aperture radar. After the launch of Sentinel-1B in 2016, two satellites had a return visit period of six days at the equator. We used all available Ground Range Detected (GRD)

100 images acquired under Interferometric Wide (IW) mode, with a spatial resolution of 10 m. The boundary noise removal, thermal noise removal, radiometric calibration and terrain correction has been conducted by the GEE with the same processing as Sentinel-1 Toolbox. Sentinel-1 data in both ascending and descending orbit were considered. For the places where two orbits were available, only the descending data was used to avoid the terrain distortion caused by the combination of two orbits. In total, over 2.7 million Sentinel images were used to cover the global terrestrial surface (Fig. S2).

### 105 2.2 Volunteered geographic information

Volunteered geographic information (VGI) is the geographic information that was created, edited and updated by volunteers (Goodchild, 2007). The well-known VGI project, OpenStreetMap (OSM), provides online maps that can be edited and used by everyone. Since its launch in 2004, OSM has been updated and maintained by seven million volunteers (Haklay and Weber, 2008). OSM has been used for positioning and navigation, urban modeling, and land cover mapping (Fonte et al.,

110 2020; Goetz, 2013; Tian et al., 2019). In fact, over 600 million buildings and roads were tagged in the OSM data

Earth System Science Data Discussions

Open Access

(https://taginfo.openstreetmap.org/keys, last access: 17 Aug 2021). These data should be important reference for ISA mapping, but unfortunately, in the current literature, they have seldom been used for ISA mapping at the global scale. Therefore, we used OSM data as a source of the training samples for the GISA-10m mapping. Specifically, we extracted the buildings and road networks as potential training samples from the OSM planet data built on January 2, 2017[1].

115 ## 2.3 Existing ISA datasets

We intercompared GISA-10m with existing datasets, including GISA, GAIA, GAUD, WSF2015, FROM_GLC10, GLCFCS, GHSL2018 (Table 1). GISA, GAIA and GAUD are Landsat-derived annual global ISA datasets for the time periods 1972-2019, 1985-2018 and 1985-2015, respectively (Gong et al., 2020b; Huang et al., 2021a; Liu et al., 2020b). GHSL2018 is a global settlement layer based on Sentinel-2 composite, where convolutional neural network was used to estimate the
120 settlement probability (Corbane et al., 2021).WSF2015 and GLCFCS are global ISA datasets based on Landsat-8 and Sentienl-1 data. WSF2015 collected samples based on a set of spectral and topographic rules, and GLCFCS derived samples from GlobeLand30 (Marconcini et al., 2020; Zhang et al., 2020a). Gong et al., (2019) generated the 10-m global land cover product FROM_GLC10 using Sentinel-2 data and the random forest classifier. It should be noted that these datasets were different for the definitions of land cover categories and mapping purposes. For instance, GHSL2018 and WSF2015 focused
125 on human settlements, while GAUD delineated urban extent (Table 1). In this study, GISA-10m monitored impervious surface area (ISA) generated by human activities, including all kinds of human settlements, transportation facilities, industries and mining places, by courtesy of the employment of high spatial resolution satellite data. Therefore, artificial impervious surface and human settlements were treated as ISA in this paper.
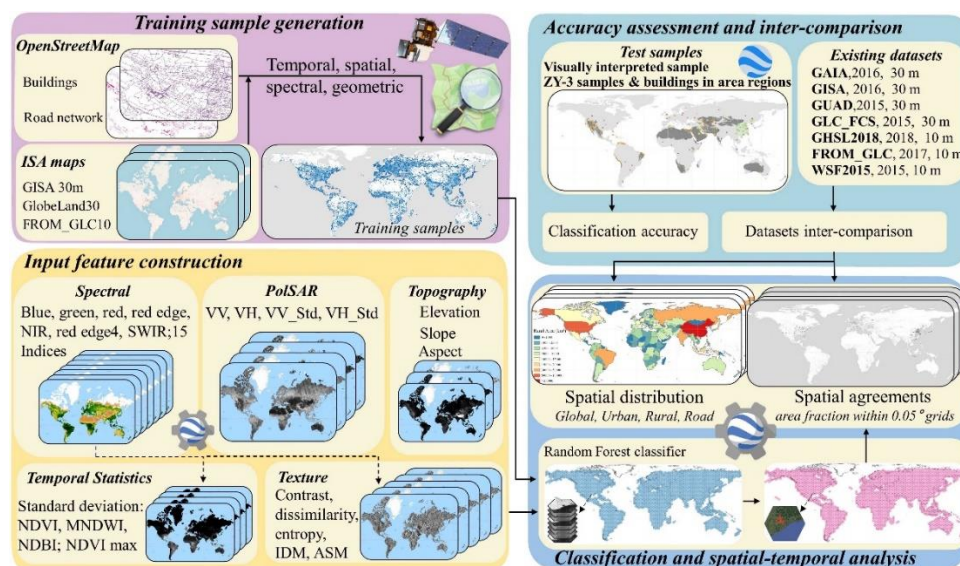
130 **Figure 1. The flowchart for GISA-10m mapping.**

3 Methodology

The main objectives of this study were to: 1) investigate the 10m global ISA mapping (GISA-10m) by combining Sentinel-1 and -2 images with other geographic information; and 2) analyse the distribution of urban and rural ISA at 10-m resolution. The flowchart for GISA-10m mapping was shown in Fig. 1, including training sample generation, multi-source feature

135   construction, random forest classification, accuracy validation and dataset comparison. Based on satellite-derived ISA maps and VGI (i.e. OpenStreetMap), we proposed a rule-based approach to automatically generate global training samples. Using more than 2.7 million Sentinel images on the GEE, multi-source features were then constructed and fed to random forest classifier to obtain the result. The accuracy of GISA-10m was assessed by visually-interpreted and the third-party samples. To better evaluate the performance of GISA-10m, we compared it with the current state-of-the-art global ISA datasets (Table

140   1). Finally, the distribution of ISA over urban and rural regions was analysed.

3.1 Global ISA mapping using multi-source geospatial data

3.1.1 Sample collection

In the case of large-scale supervised classification, both the quantity and quality of samples are important (Foody and Arora, 1997). ISA is a highly variable object, and its attributes in the Sentinel-2 multispectral images are related to materials,

145   viewing angles, and atmospheric conditions, while its response to the Sentinel-1 SAR depends on dielectric properties, geometry, and surface roughness. Hence, a large number of training samples were required to address the aforementioned challenges that would be encountered at the global scale. Training samples were usually acquired by means of visual interpretation or automatic extraction from existing datasets. The visual interpretation methods were labour and time intensive, even for small regions. Therefore, at a large scale, training samples were usually extracted from existing datasets

150   with similar temporal and spatial coverage. However, the sample quality was affected by the quality of the datasets used (Jokar Arsanjani et al., 2016; Wessels et al., 2016). Theoretically, samples extracted from single dataset may result in more errors and uncertainties, while multiple sources can improve the reliability of training samples (Huang and Zhang, 2013). We thus proposed to collect global training samples by incorporating existing ISA datasets and crowdsourcing OSM. To concisely distinguish the two types of ISA samples, we named the ISA sample extracted from the existing satellite-derived

155   ISA dataset as ISA_{RS} and those extracted from the OSM as ISA_{OSM}.

The existing ISA datasets generally covered broad terrestrial surface, but they were different in term of definitions, spatial resolutions, and temporal coverage. In this study, GISA, FROM_GLC10, and GlobeLand30 were chosen to extract training samples due to the following reasons: 1) GISA aimed at mapping global impervious surface area, which was consistent with GISA-10m; 2) GlobeLand30 employed extensive visual interpretation to detect artificial surfaces, which can effectively

160   reduce false alarms from other datasets (Chen et al., 2015); 3) The definition of FROM_GLC10 (impervious surface) was also consistent with GISA-10m and its spatial resolution was 10 m. GHSL2018, WSF2015 and GAUD were not considered

since they aimed to outline human settlements or urban extents (Table 1). We then collected the eligible training samples according to the following rules.

(1) Temporal rule: GISA was a global ISA dataset during 1972–2019, and we selected its result of 2016 to match the time

165 when Sentinel data was used in this research. GlobeLand30 documented global land cover map for 2000, 2010 and 2020, and here, the 2010 map was chosen. Although the 2020 map was more recent to 2016, it contained ISA that was built after 2016, making it unsuitable for GISA-10m mapping. The following spatial and spectral rules were used to remove the possible errors.

(2) Spatial rule: We first checked the class labels of the three datasets at each pixel. If these labels were the same (i.e. ISA),

170 the pixel was taken as a potential ISA_{RS} sample. The collaboration of multiple datasets can effectively reduce the errors that existed in a single dataset. In addition, we filtered out the edge pixels in each dataset to reduce the uncertainty, since they were more likely to be mixed pixels.

(3) Spectral rule: After the above steps, there may still be a small amount of errors in the current samples. Hence, we applied the spectral rule to remove these erroneous samples. Specifically, we measured the mahalanobis distance between each

175 ISA_{RS} sample to the spectral average of each hexagon (the mapping unit adopted in this study), and filtered out the samples with distance greater than $\mu + \delta$ (μ and δ represents the mean and standard deviation, respectively) (Huang et al., 2021a). Vegetation and water bodies were common false alarms in existing datasets (Figs. 2a&b). However, these errors often accounted for a relatively small proportion, and they can be effectively identified and reduced by the spectral rule. It can be seen that most of the water bodies and vegetation (e.g. red rectangles in Fig. 2) were successfully removed from the initial
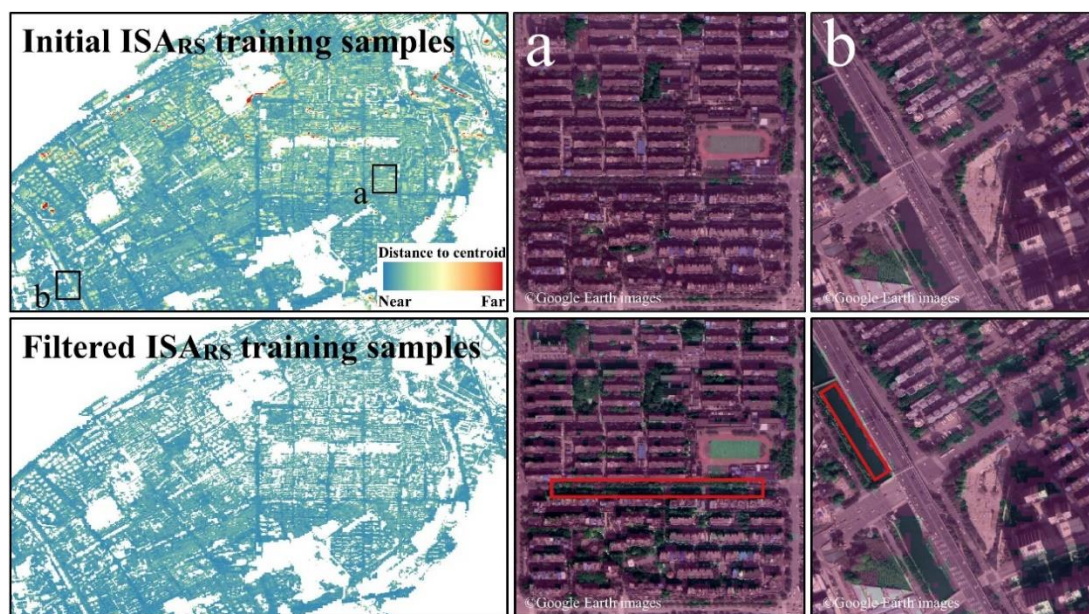
180 ISA_{RS} training samples.

Figure 2. The example of initial and filtered ISA_{RS} training samples in Wuhan city (30.625382° N, 114.392682° E). The purple in the close-up maps represents the samples.

On the other hand, we extracted ISA$_{OSM}$ samples from OSM buildings and roads through the following rules.

185 (1) Temporal rule: We chose the OSM data built on 2 January, 2017 in terms of the time of GISA-10m. This version of OSM data was employed to ensure that buildings and roads were constructed in 2016 or before, and hence, it was suitable for 2016 ISA mapping.

(2) Geometric rule: A natural way to extract training points from OSM was to generate random points within the building or road polygons (Johnson and Iizuka, 2016; Liu et al., 2020a). However, random points may contain erroneous or mixed pixels.

190 Such problems can be mitigated by making negative buffers to the polygons (Liu et al., 2020a). However, this approach was very time-consuming when applied to global ISA mapping, especially given more than 200 million buildings in the OSM data. Therefore, in this study, we extracted the geometric center of a building polygon as an ISA$_{OSM}$ sample, which was more efficient than buffering and random points. Notably, although we can filter out the erroneous buildings using attribute tags (e.g. dams, swimming pools, playgrounds), the geometric center of a building was not always an ISA sample. Hence, we

195 further required that the geometric center must be contained by the building. As in Figs. 3a&b, the incorrect building geometric centers (e.g., the vegetation and water, indicated by the yellow points) were successfully identified and removed by the geometric rule. In addition, we excluded buildings with area less than 100 m^2 (~ a Sentinel pixel).

Compared with the widely used 30-m Landsat data, the high-resolution Sentinel data promotes a better delineation of roads. We thereby also extracted ISA$_{OSM}$ samples from the OSM road networks. The OSM roads usually consisted of centerlines rather than boundaries. Therefore, we extracted the center point of each road rather than its geometric center, as the road ISA

200 samples. Given that the width of low-grade roads may be smaller than 10 m (a Sentinel pixel), we kept only the main roads (highway="primary").
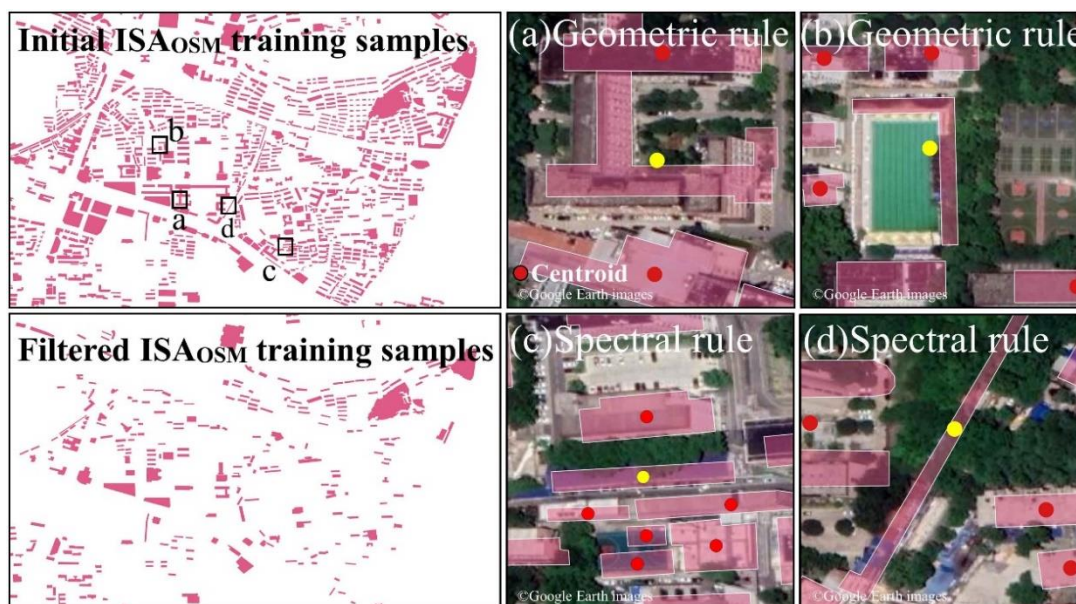
Figure 3. Examples of initial and filtered ISA$_{OSM}$ training samples in Wuhan city (30.530202° N, 114.356287° E). The yellow points
205 **in the close-up maps represent the errors recognized by (a-b) geometric and (c-d) spectral rules.**

(3) Spatial rule: Given the uneven spatial distribution of OSM data (Tian et al., 2019), we then applied the spatial rule to balance its distribution at the global scale. Specifically, for hexagons with more than 10,000 OSM records (i.e. buildings and roads), we randomly selected 10,000 records as initial samples. The dilution of OSM data can significantly reduce subsequent computational cost. In addition, considering that ISA_{OSM} could overlie with ISA_{RS}, we removed the ISA_{OSM}

210   samples that were intersected with ISA_{RS}.

(4) Spectral rule: Although OSM uses human as sensors, ISA_{OSM} samples may still contain erroneous points, such as vegetation and water body beside roads. As shown in Figs. 3c&d, the yellow points satisfied the temporal, spatial and geometric rules, but they were actually vegetation. Hence, we applied the spectral rule to filter them out. Specifically, the ISA_{OSM} samples whose MNDWI (modified normalized difference water index) or NDVI (normalized difference vegetation

215   index) values larger than $\mu+\delta$ were removed (μ and δ represent the mean and standard deviation of the indices, respectively), as these points were more likely to be vegetation or water body (Huang et al., 2021a).

After obtaining the ISA candidate samples, we randomly selected 2,500 ISA_{RS} and ISA_{OSM}, respectively, within each hexagon as the final ISA training samples (see Section 5.3 for details). It can be seen that our generated ISA samples covered broad terrestrial surface, especially in India and China where a large number of small villages gather (Fig. 4).
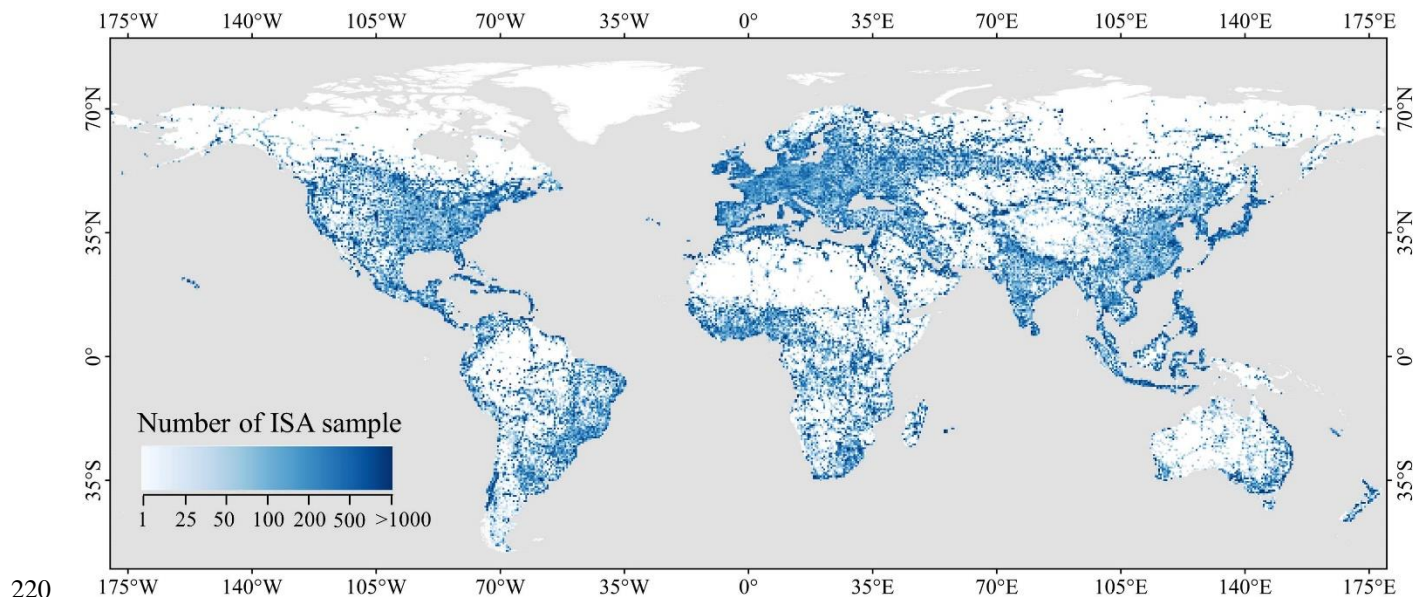

Figure 4. Global distribution of ISA training samples. The number of samples was counted within 0.5º spatial grid.

On the other hand, NISA (non-ISA) training samples were also important for accurate ISA mapping. We used the three existing datasets (i.e. GISA 30m, FROM_GLC10, GlobeLand30) and OSM to generate the NISA samples. Firstly, we took the intersect of the NISA regions in the three datasets as the initial NISA sample pool:

225    $NISA = NISA_{GISA} \cap NISA_{GlobeLand30} \cap NISA_{FROM\_GLC10} - ISA_{OSM}$ (1)

For GlebeLand30 and FROM_GLC10, NISA was defined as all land cover type other than ISA. We then masked the initial NISA sample pool using OSM buildings and roads to suppress the errors in the existing global dataset. To this end, here we used the OSM version built in December 2020[2], which documented more buildings and road networks than the 2017 version. Besides, we buffered the OSM roads with 30 m to better mitigate the errors. Subsequently, 30,000 points were randomly selected in each hexagon as NISA samples. The distance between each NISA sample was kept larger than 200 m to ensure its diversity and irrelevance. Finally, we extracted 58 million training samples (51,674,533 NISA and 6,897,378 ISA samples) for GISA-10m mapping.

Table 2. The multi-source features used for GISA-10m mapping.

Type	Features	Description	Dimension	Source
Spectrum	Blue, green, red, red edge1, red edge2, red edge3, NIR, red edge4, SWIR1 and SWIR2	50th percentile value of reflectance derived from all available Sentinel-2 images	10	Sentinel-2
Normalized indices	Index1, Index2, Index3, Index4, Index5, Index6, Index7, Index8, Index9, Index10, Index11, Index12, Index13, Index14, Index15	Normalized indices derived from the spectral bands described above. The indices are calculated as: Index1=NI (NIR, blue), Index2=NI (NIR, green), Index3=NI (NIR, red), Index4=NI (NIR, red edge1), Index5=NI (NIR, red edge2), Index6=NI (NIR, red edge3), Index7=NI (NIR, red edge4), Index8=NI (SWIR1, blue), Index9=NI (SWIR1, green), Index10=NI (SWIR1, red), Index11=NI (SWIR1, NIR), Index12=NI (SWIR2, blue), Index13=NI (SWIR2, green), Index14=NI (SWIR2, red), Index15=NI (SWIR2, NIR), where NI represents the function (b1- b2) / (b1+ b2), b1 and b2 denote two spectral bands	15	Sentinel-2
SAR	VV, VH	Temporal mean VV and VH backscatter coefficients of Sentinel-1 images	2	Sentinel-1
Temporal statistics	NDVI_Std, MNDWI_Std, NDBI_Std, NDVIMax, VV_Std, VH_Std	Standard deviation of NDVI, MNDWI, NDBI, VV and VH backscatter coefficients; Maximum NDIV of the year	5	Sentinel-1& Sentinel-2
Texture	Contrast, dissimilarity, entropy, IDM, ASM	The GLCM texture derived from NIR band of Sentinel-2 data, including entropy, dissimilarity, contrast, angular second moment (ASM) and inverse difference moment (IDM)	5	Sentinel-2
Topography	Elevation, slope and aspect	Slope and aspect calculated from the elevation	3	SRTM & GMTED

3.1.2 Multi-source feature extraction

The dedicated image pyramid of GEE enabled us to perform pixel-wise feature extraction (Gorelick et al., 2017; Huang et al., 2021a; Yang and Huang, 2021). Therefore, based on all available Sentinel data in 2016, we constructed a set of spectral, phenological, texture, SAR and topographical features with the temporal composite method (Table 2). This approach used all

---

[2] https://planet.openstreetmap.org/planet/2020/planet-201207.osm.bz2, last access: 13 Mar 2021

available data and at the same time allowed us to reduce the feature dimension, preserve the temporal information and minimize the effects from clouds and shadows (Yang and Huang, 2021). Firstly, the 50th percentile TOA reflectance was

240 calculated for each spectral band (Table 2). Moreover, we calculated 15 spectral indexes to improve the discrimination between ISA and NISA (Table 2). These indices were built according to the following criteria: (1) They were mainly constructed by near-infrared (NIR) and short-wave infrared (SWIR) bands due to their better atmospheric transmission (Huang et al., 2021a; Yang and Huang, 2021); (2) Each index contained at least one 10-m band (i.e. visible and NIR bands) to ensure the spatial resolution of the features. To further exploit the textural information for the ISA mapping, we computed

245 the gray-level co-occurrence matrix (GLCM) via NIR band (Weng, 2012). Owing to the high redundancy among GLCM measurements (Clausi, 2002; Zhang et al., 2020a), we chose the contrast, dissimilarity, entropy, IDM (inverse difference moment) and ASM (angular second moment) for texture extraction (Conners et al., 1984; Haralick et al., 1973; Rodriguez-Galiano et al., 2012). The window size for GLCM measurements was set to 7×7 as it was suitable for urban classification with image resolution from 2.5 to 10 m (Puissant et al., 2005). Besides, we averaged the GLCM from different directions (0,

250 45, 90, and 135) to maintain the rotational invariance (Rodriguez-Galiano et al., 2012).

Given that spectral responses of vegetation and water bodies vary over time, we calculated the maximum NDVI as well as standard deviation of NDVI, MNDWI, and NDBI (normalized difference built-up index) to further enhance the temporal information (Tucker, 1979; Xu, 2006; Zha et al., 2003). These temporal characteristics were useful in identifying NISA with temporal fluctuations. For example, the spectra of fallow cropland and ISA were similar, even SAR data may not well

255 separate them. However, the NDVI of cropland can describe the changes of crops growth, and hence, its standard deviation can be used to distinguish between ISA and cropland. In addition, to increase the robustness of these temporal features, Sentinel-2 data from adjacent two years were also included.

With regard to the SAR data, the VV (vertical-vertical polarization) and VH (vertical-horizontal polarization) backscatter coefficients from the Sentienl-1 images were selected. Specifically, based on all available Sentienl-1 data, the annual mean

260 and standard deviation of the VV and VH backscatter coefficients were calculated by the temporal composite method:

$$\sigma_{mean} = \frac{1}{n}\sum_{i=1}^{n}\sigma_i \tag{2}$$

$$\sigma_{std} = \sqrt{\frac{\sum_{i=1}^{n}(\sigma_i - \sigma_{mean})^2}{n}} \tag{3}$$

where n denotes the total number of Sentinel-1 observations within a year and σ_i represents the ith backscatter coefficient observation in the year. The temporal mean method can reduce speckle noise in the SAR images (Lin et al., 2020), while the

265 annual standard deviation can reflect temporal information. In addition, DEM-derived (Digital Elevation Model) topographic features were also constructed to reduce false alarms induced by SAR data over mountain areas (Ban et al., 2015; Gamba and Lisini, 2013). Specifically, we used SRTM (Shuttle Radar Topographic Mission) in the areas below 58° latitude and GMTD2010 (Global Multi-resolution Terrain Elevation Data 2010) in the areas above 58° (Huang et al., 2021a). Finally, a total of 41 features were constructed on the 2.7 million Sentinel images (2,613,180 Sentinel-2 and 122,156 Sentinel-1) and

270 DEM data.

3.1.3 Hexagon-based adaptive random forest classification

When dealing with global land cover classification, the global terrestrial surface was usually divided into homogeneous sub-regions according to criteria such as climate, land cover or administrative regions (Goldblatt et al., 2018; Homer et al., 2004; Turner, 1989). For global ISA mapping, regular square grids were commonly used (Table 1), such as 1° and 5° grids (e.g. WSF2015 and GLCFCS). Herein we divided the terrestrial surface into 2° hexagonal grids (Fig. 1), due to its symmetry and invariance (Birch et al., 2007; Goldblatt et al., 2018; Huang et al., 2021a). Besides, there were no gaps or overlaps between hexagons, and the distance between adjacent hexagon centers was approximately equal (Richards et al., 2000).

Random forest (RF) classifier has been widely used in global ISA mapping, due to its robustness to erroneous samples, flexibility to high-dimensional data and tolerance to noise (Bauer and Kohavi, 1999; Wulder et al., 2018) (Table 1). It utilizes ensemble learning to obtain predictions by voting on categories through multiple decision trees (Breiman, 2001). Each tree uses a random subset of the input features to increase the generalization ability. In addition, trees are grown from different subsets of training data (i.e. bagging or bootstrap) to increase the diversity (Rodriguez-Galiano et al., 2012). RF has been proved to outperform other classifiers when dealing with large-scale and high-dimension data (Gislason et al., 2006; Goldblatt et al., 2016). The flexibility of RF to handle multi-source data also makes it convenient for us to deal with Sentinel radar and optical data. Therefore, together with the aforementioned multi-source features and global training samples, RF was used for GISA-10m mapping. As suggested by Yang and Huang, (2021), the number of trees was set to 200.

3.2 Accuracy assessment

The test samples of GISA-10m included (1) visually interpreted samples via Google Earth, (2) test samples extracted from the ZiYuan-3 (ZY-3) built-up datasets (Liu et al., 2019), and (3) building samples located in the arid areas.

(1) As suggested by Stehman and Foody (2019), we used cluster sampling to collect the visually-interpreted test samples. The primary sampling unit involved 59 grids with a side length of 1°, which was randomly selected based on population, ecoregion, and urban landscape (red squares in Fig. 5). The secondary sampling unit included the random samples within each grid. Specifically, in each grid, we randomly selected 100 ISA and 100 NISA points to test their accuracy. An equal allocation of ISA and NISA test samples could reduce the bias of the accuracy assessment and hence allow for a more accurate estimate of user's accuracy (Marconcini et al., 2020; Olofsson et al., 2014; Stehman, 2012; Story and Congalton, 1986; Wehmann and Liu, 2015). By referring to the high-resolution Google Earth images, a pixel (10m × 10m) was labelled as ISA if more than half of its area was cover by ISA, otherwise it was identified as NISA. In such way, a total of 10,800 test samples were obtained.

(2) Liu et al., (2019) proposed a multi-angle built-up index to extract built-up areas from ZY-3 images covering 45 global cities, with an overall accuracy greater than 90%. The multi-angle ZY-3 images depicted the three-dimensional and vertical structure of buildings, which were more effective and accurate than the planar feature extraction for detecting built-up areas. Given the higher spatial resolution (2 m) and better accuracy of ZY-3 global built-up dataset, we extracted test samples from

it in the year of 2016 (Huang et al., 2021a; Liu et al., 2019). A sample (10m × 10m) was labeled as ISA if more than 50% of its area was classified as ISA in the ZY-3 dataset, while NISA samples were those with no built-up pixels in the area (Huang et al., 2021a). For each city, the number of samples was proportional to the area of the ZY-3 image, and the ratio of ISA and NISA test samples was consistent with the ratio of the built-up and non-built-up (Huang et al., 2021a). In this way, we obtained 47,216 NISA and 21,152 ISA samples (green dots in Fig. 5) from 24 cities in the ZY-3 built-up dataset.

(3) Considering the difficulty of ISA extraction in the arid regions (Tian et al., 2018), we paid special attention to the accuracy assessment in the arid regions. To this end, we visually interpreted 5,385 building pixels in these regions. A total of 25 photo interpreters were recruited for this task by referring to the Google Earth images. These samples were further checked by three experts. The arid regions were defined according to the "Deserts and Xeric Shrublands" biome in Olson et al., (2001).

Based on the three groups of test samples aforementioned, the accuracy of GISA-10m was assessed by overall accuracy (OA), kappa, producer's accuracy (PA), user's accuracy (UA), and F-Score (the harmonic mean of PA and UA).
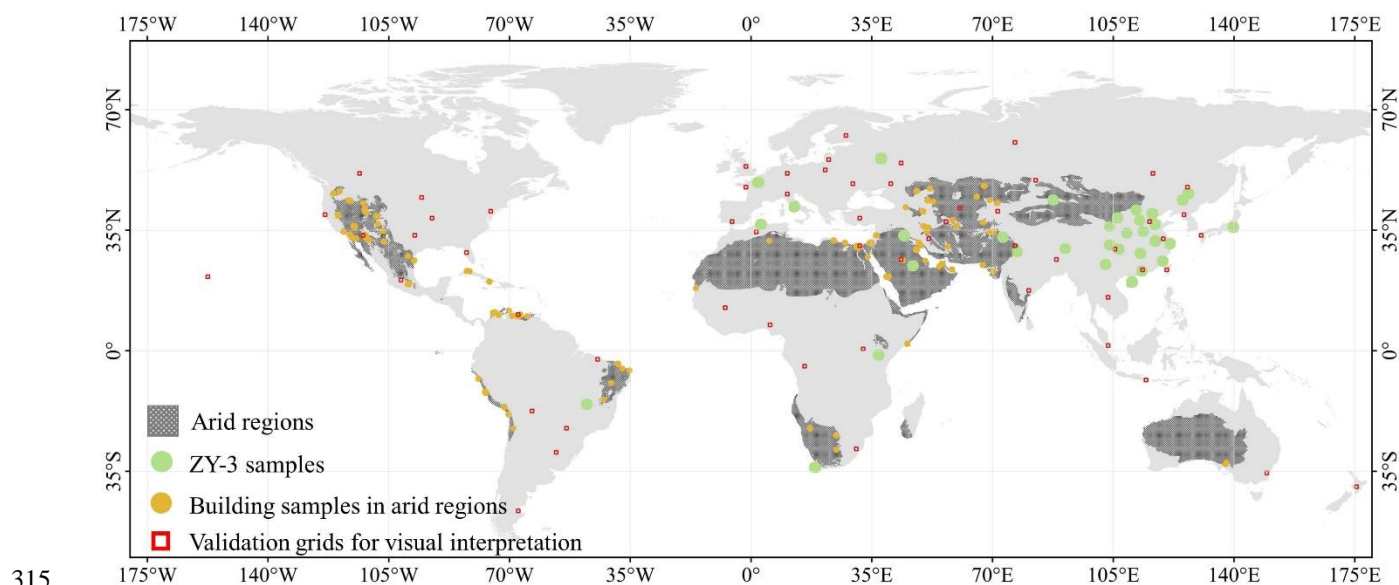

Figure 5. Global distribution of the test samples and grids used in this study, including (1) 59 grids for visual interpretation, (2) ZY-3 reference set covering 23 cities, and (3) 5,385 building samples in the arid regions. The arid regions were extracted from "Deserts and Xeric Shrublands" biome in Olson et al., (2001).

3.3 Inter-comparison between different global datasets

Seven existing global ISA datasets were used for inter-comparison with GISA-10m, including GHSL2018, GLCFCS, WSF2015, FORM_GLC10, GISA, GAUD, and GAIA (Table 1). First, the three groups of test samples mentioned above were used to assess and compare the accuracy of these products. Second, their spatial agreements with GISA-10m were measured by the linear fit of ISA fraction, including metrics such as correlation coefficient and root mean square error (RMSE). Finally, attention was paid to their performances in urban and rural regions for a comprehensive assessment.
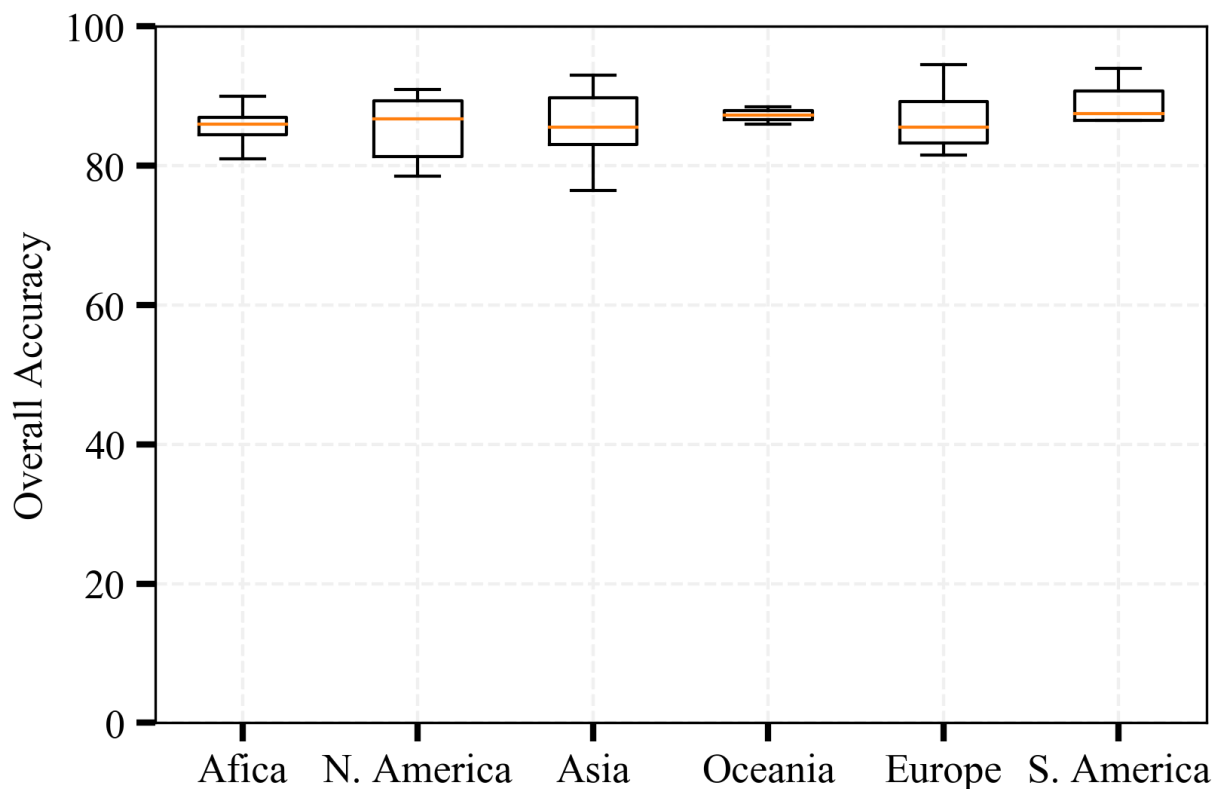
Figure 6. Box plots of the overall accuracy for GISA-10m in the six continents.

4 Results

4.1 Accuracy assessment of GISA-10m

4.1.1 Global scale

The accuracy assessment based on the visually-interpreted samples were shown in the Table 3. GISA-10m exhibited the highest OA of 86.06%, with an increase of +2.73%, +3.73% and +2.3%, respectively, with respect to GHSL2018, GLCFCS and WSF2015 (Table 3). The Kappa of GISA-10m was 0.7165, which exceeded the WSF2015, FROM_GLC10 and GAIA by 0.052, 0.1774 and 0.2039, respectively. Alongside, GISA-10m showed higher accuracy as to the 30 m datasets (i.e. GISA, GAUD, GAIA), which suggested a better delineation of global ISA due to its higher resolution. Fig. 6 summarized the results of the accuracy assessment at the continent level, with the average and standard deviation of OA for each continent shown in the box plots. In general, GISA-10m exhibited stable performance for each continent, with an average OA more than 85%. Specifically, Oceania and South America obtained the best OA of 87.25% and 87.08%, followed by Europe (86.45%) and Asia (85.85%).

340 **Table 3. Results of quantitative accuracy assessment via visually-interpreted and ZY-3 samples between GISA-10m and the existing ISA datasets. OA represents the overall accuracy.**

Globe	Visually interpreted samples (n=10800)				ZY-3 samples (n=68368)			
	OA (%)	Kappa	F-Score of ISA (%)	F-Score of NISA (%)	OA (%)	Kappa	F-Score of ISA (%)	F-Score of NISA (%)
GISA-10m	**86.06**	**0.7165**	**83.65**	**88.55**	**86.25**	**0.6664**	76.25	**90.32**
GHSL2018	83.33	0.6540	78.66	86.89	84.53	0.6401	75.27	88.74
GLCFCS	82.33	0.6336	77.57	85.96	84.56	0.6280	73.68	89.08
WSF2015	83.76	0.6645	79.68	87.06	85.44	0.6664	**77.35**	89.27
FROM_GLC10	78.16	0.5391	69.65	83.39	83.66	0.6082	72.39	88.39
GISA	78.84	0.5532	70.65	83.88	85.63	0.6627	76.65	89.63
GAUD	77.36	0.5185	67.46	83.01	85.59	0.6549	75.70	89.76
GAIA	77.05	0.5126	67.13	82.77	84.23	0.6381	75.39	88.40

GISA-10m obtained the best OA of 86.25% on the ZY-3 samples, outperforming GHSL2018, GLCFCS and WSF2015, by 1.72%, 1.69% and 0.81%, respectively. The ZY-3 images employed by Liu et al., (2019) covered 45 major global cities, and therefore the ZY-3 samples were more inclined to reflect the accuracy in urban regions. Therefore, the accuracy difference between various datasets was not significant (Table 3). Due to the relatively coarser resolution, the 30 m datasets usually tended to overestimate the ISA extent (Gong et al., 2020b), resulting in higher UA but lower PA (Table S1). For example, the ISA UA of GISA was slightly higher than GISA-10m, but its PA was much smaller than the latter (Table S1). However, when the two metrics (PA and UA) were considered at the same time (i.e. F-Score), GISA-10m outperformed GISA.

4.1.2 Rural and arid regions

The population of rural regions is comparable to that of urban regions (https://data.worldbank.org/). Existing studies as well as their global ISA datasets usually focus on the performance in urban regions, but the accuracy of rural ISA regions has not been sufficiently assessed. Hence, in this study, we paid special attention to the accuracy assessment in the global rural regions. Specifically, we divided the GISA-10m into urban and rural regions using the urban boundary defined by Li et al., (2020). In fact, due to the random sampling strategy, most of visually-interpreted test samples were located in rural regions. In the case of the visually-interpreted samples, GISA-10m exhibited a better OA of 86.19% against the GHSL2018 (84.92%), GLCFCS (83.25%), FROM_GLC10 (78.83%) and WSF2015 (83.81%). As regards the three 30-m datasets (i.e. GISA, GAIA, GAUD), their ISA accuracy (F-Score) decreased significantly in the rural regions while the NISA accuracy was relatively stable (Tables 2&3). Having a closer look at the PA, one can notice that the ISA PA decreases by more than 15% for all the three 30-m datasets (Table S2), which suggested their more omission errors in the rural regions (Fig.12b). This demonstrated the deficiency of 30-m datasets in depicting rural ISA and also reflected the importance of 10-m global ISA mapping.

Table 4. Results of quantitative accuracy assessment via visually-interpreted and ZY-3 samples in rural regions between GISA-10m and the existing ISA datasets. OA represents the overall accuracy.

Rural Regions	Visually interpreted samples (n=9547)				ZY-3 samples (n=43950)			
	OA (%)	Kappa	F-Score of ISA (%)	F-Score of NISA (%)	OA (%)	Kappa	F-Score of ISA (%)	F-Score of NISA (%)
GISA-10m	**86.19**	**0.6794**	**77.96**	**90.48**	**90.85**	**0.4768**	52.46	**94.94**
GHSL2018	84.92	0.6297	73.34	89.88	88.95	0.4656	**52.82**	93.74
GLCFCS	83.25	0.5871	70.15	88.72	89.46	0.4261	48.33	94.13
WSF2015	83.81	0.6012	71.17	89.12	89.37	0.4514	51.05	94.04
FROM_GLC10	78.83	0.4485	57.08	86.24	88.59	0.3884	45.08	93.63
GISA	77.87	0.4082	52.53	85.80	89.83	0.3954	44.66	94.40
GAUD	76.38	0.3516	46.13	85.05	89.70	0.3199	36.35	94.40
GAIA	75.41	0.3213	43.05	84.49	88.93	0.3611	41.85	93.88

365   **Table 5. Results of quantitative accuracy assessment via visually-interpreted and ZY-3 samples in arid regions between GISA-10m and the existing ISA datasets. OA represents the overall accuracy.**

Arid Region	Visually interpreted samples (n=1020)				ZY-3 samples (n=10827)			
	OA (%)	Kappa	F-Score of ISA (%)	F-Score of NISA (%)	OA (%)	Kappa	F-Score of ISA (%)	F-Score of NISA (%)
GISA-10m	**86.67**	**0.7358**	86.05	**88.22**	**89.64**	**0.7296**	**79.95**	**93.01**
GHSL2018	86.57	0.7336	**86.06**	87.99	85.13	0.5817	67.68	90.34
GLCFCS	82.16	0.6454	80.32	84.46	85.14	0.6232	72.45	89.82
WSF2015	82.45	0.6516	80.95	84.56	88.37	0.6881	76.53	92.27
FROM_GLC10	76.27	0.5271	70.97	80.59	84.06	0.5755	68.18	89.37
GISA	80.20	0.6058	76.89	83.39	87.72	0.6795	76.23	91.72
GAUD	77.06	0.5424	71.88	81.20	88.66	0.6894	76.37	92.54
GAIA	77.45	0.5506	72.84	81.35	85.78	0.6317	72.79	90.37

Furthermore, we focused on the accuracy assessment in arid regions. In general, the OA of GISA-10m was higher than the existing datasets (Table 5). Although its ISA UA did not always outperform other datasets, GISA-10m achieved the highest PA among the existing ones (Table S3). Specifically, GISA-10m exhibited a notably higher ISA PA compared to GLCFCS, FROM_GLC10, GISA, GAUD and GAIA (Table S3), indicating its better ability of detecting ISA in arid regions (Fig. 7). Moreover, the accuracy of these global ISA products was assessed using our manually and randomly chosen rural building samples (see Section 3.2). It can be found that GISA-10m extracted detected 15% more buildings in arid regions with respect to FROM-GLC10, GAUD and GAIA (Table S4), which again verified its better performance in describing rural ISA.

16
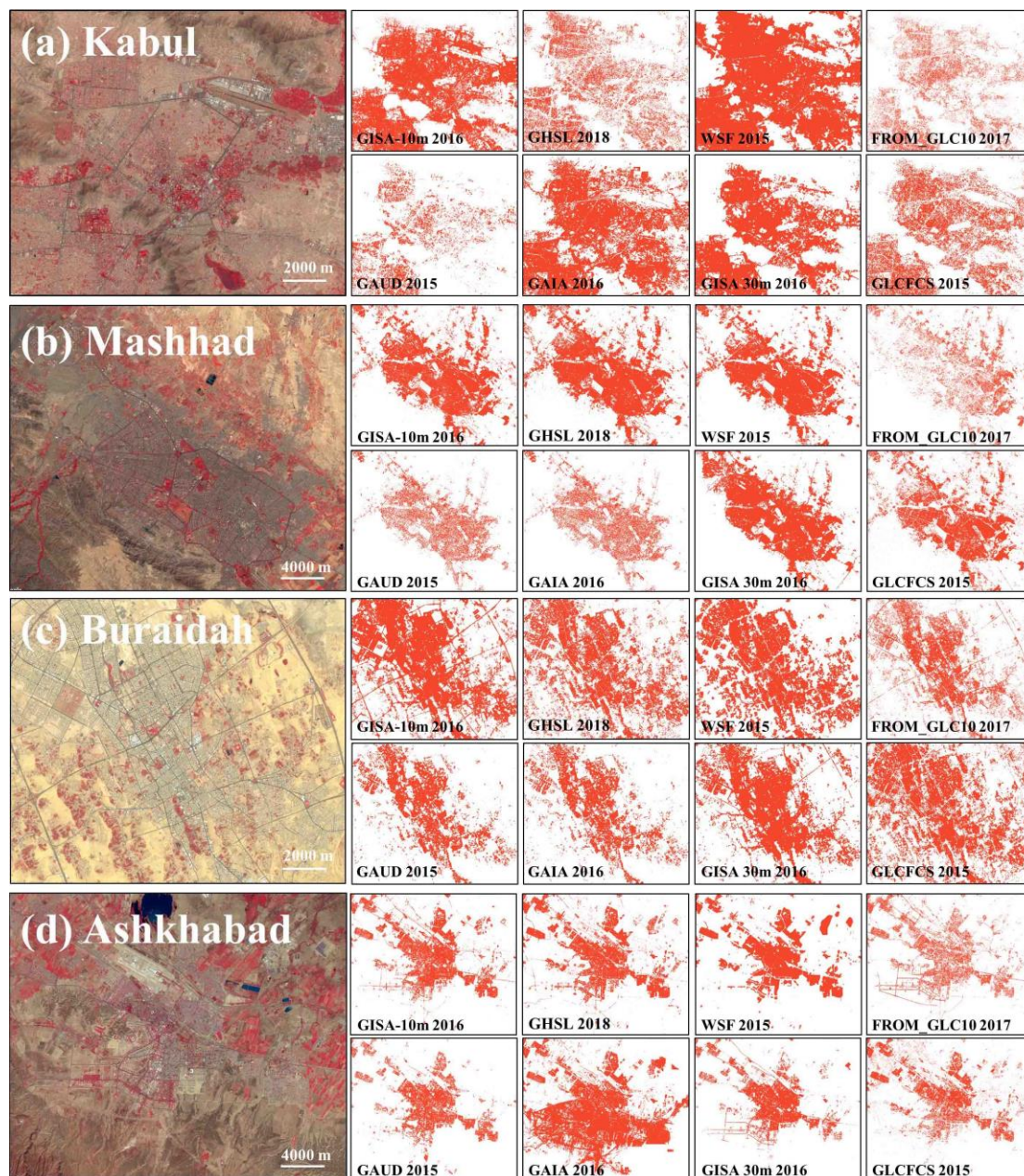
375 **Figure 7. Comparison of the GISA-10m and other datasets over arid regions in (a) Kabul, Afghanistan; (b)Mashhad, Iran; (c) Buraidah, Saudi Arabia; (d) Ashkhabad, Turkmenistan. The illustration is of Sentinel-2 images with false-color combination (R: NIR, G: Red, B: Green) to enhance the ISA.**
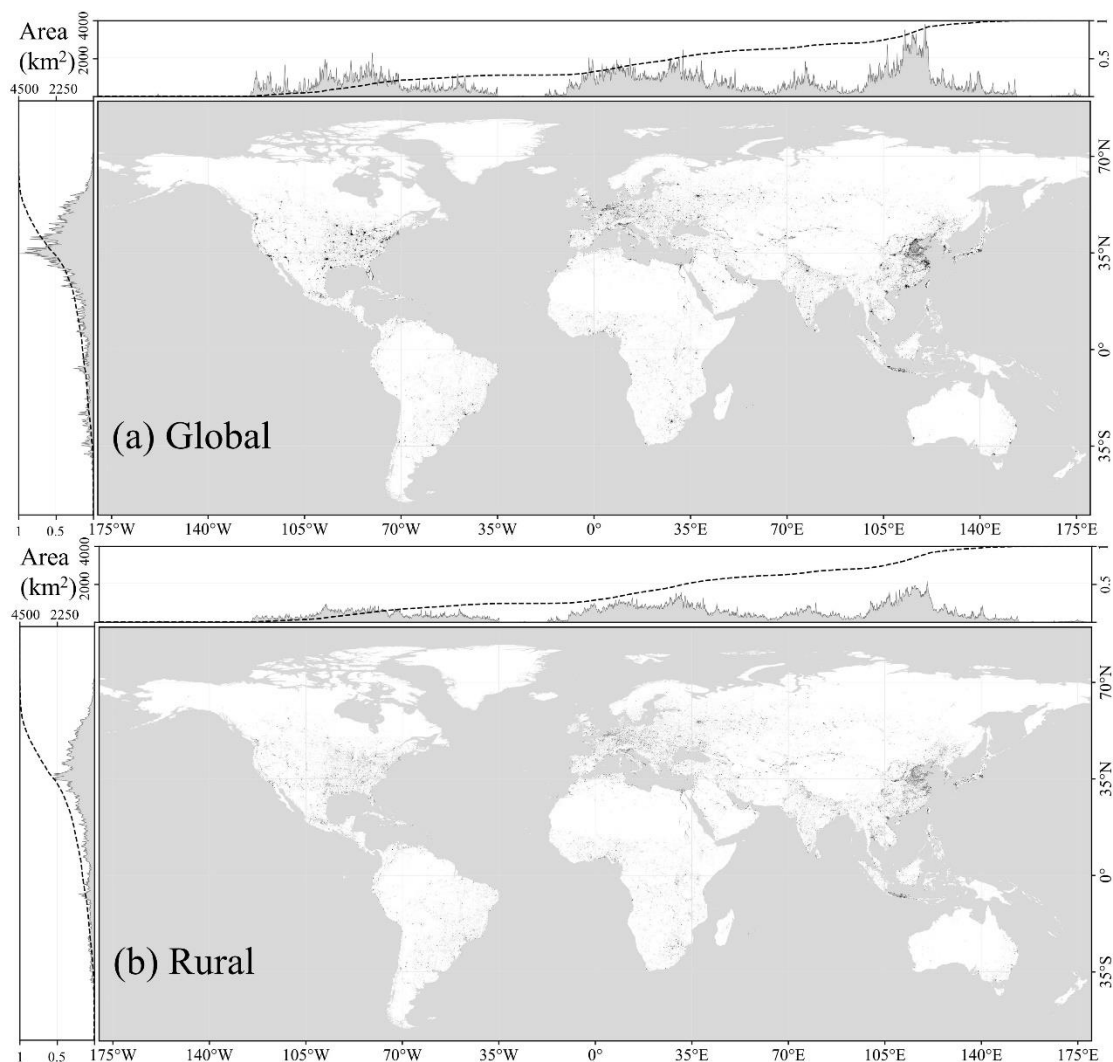
Earth System
Science
Data

Open Access

Discussions

4.2 Global ISA distribution

4.2.1 Urban and rural ISA

380   Based on GISA-10m, we analyzed the global ISA distribution at 10-m scale (Fig. 8). Global ISA was mainly distributed in Asia (41.43%), North America (20.59%), Europe (18.93%), followed by Africa (9.78%) and South America (7.50%). It was found that 67% of global ISA was located in the Eastern Hemisphere, while 85% of ISA was distributed in the north of the equator. Rural ISA was more scattered than urban ISA (Fig. 8), and it was mainly located in Asia (42.84%), Europe (19.49%) and North America (16.51%). Asia embraced the largest urban ISA, more than twice as Europe. Although North America

385   only accounted for 20% of global ISA, its urban ISA took up more than 29% of the global total. Taking a closer look at the ratio of rural and urban ISA (Table 6), one can see that rural ISA were 2.2 times larger than the urban. At the continental level, Africa possessed the highest "rural-to-urban ratio", which may be related to its large population but relatively poor economy.

Table 6. Impervious surface area derived from GISA-10m in the six continents.

ISA	Europe	Africa	S. America	Oceania	N. America	Asia	Globe
Total (10^5km^2)	1.88 (18.93%)	0.97 (9.78%)	0.75 (7.50%)	0.18 (1.76%)	2.05 (20.59%)	4.12 (41.43%)	9.94 (100%)
Rural (10^5km^2)	1.33 (19.49%)	0.78 (11.43%)	0.55 (8.11%)	0.11 (1.62%)	1.13 (16.51%)	2.93 (42.84%)	6.84 (100%)
Urban (10^5km^2)	0.55 (17.69%)	0.19 (6.16%)	0.19 (6.17%)	0.07 (2.07%)	0.92 (29.56%)	1.19 (38.35%)	3.10 (100%)
Rural/Urban	2.42	4.08	2.89	1.73	1.22	2.46	2.20

Figure 8. Spatial distribution of ISA in (a) the global and (b) rural regions. The pixel represents the ISA regions in 0.01° grid while the doted lines denote the cumulative histograms.

China and the United States (US) embraced 33% of global ISA. Together with Russia, Brazil, India, Japan, Indonesia, France, Canada and Germany, these ten countries accounted for 58% of the world. The urban ISA owned by the top ten countries (US, China, Russia, Brazil, Japan, India, Mexico, France, Germany, and the United Kingdom) took up 69% of the global total, while the top ten countries in terms of rural ISA (China, US, Russia, Brazil, India, Indonesia, Japan, France, Canada, and Germany) accounted for only 54% of the total. In Africa, the Republic of South Africa had much more urban ISA than other countries. However, Nigeria showed comparable rural ISA to the South Africa (~7738 km^2). China ranked first in term of rural ISA, most of which was located in the North China Plain (Fig. 9b). Indonesia also possessed much rural ISA, since it ranked sixth in the rural ISA but its urban ISA only ranked sixteenth.
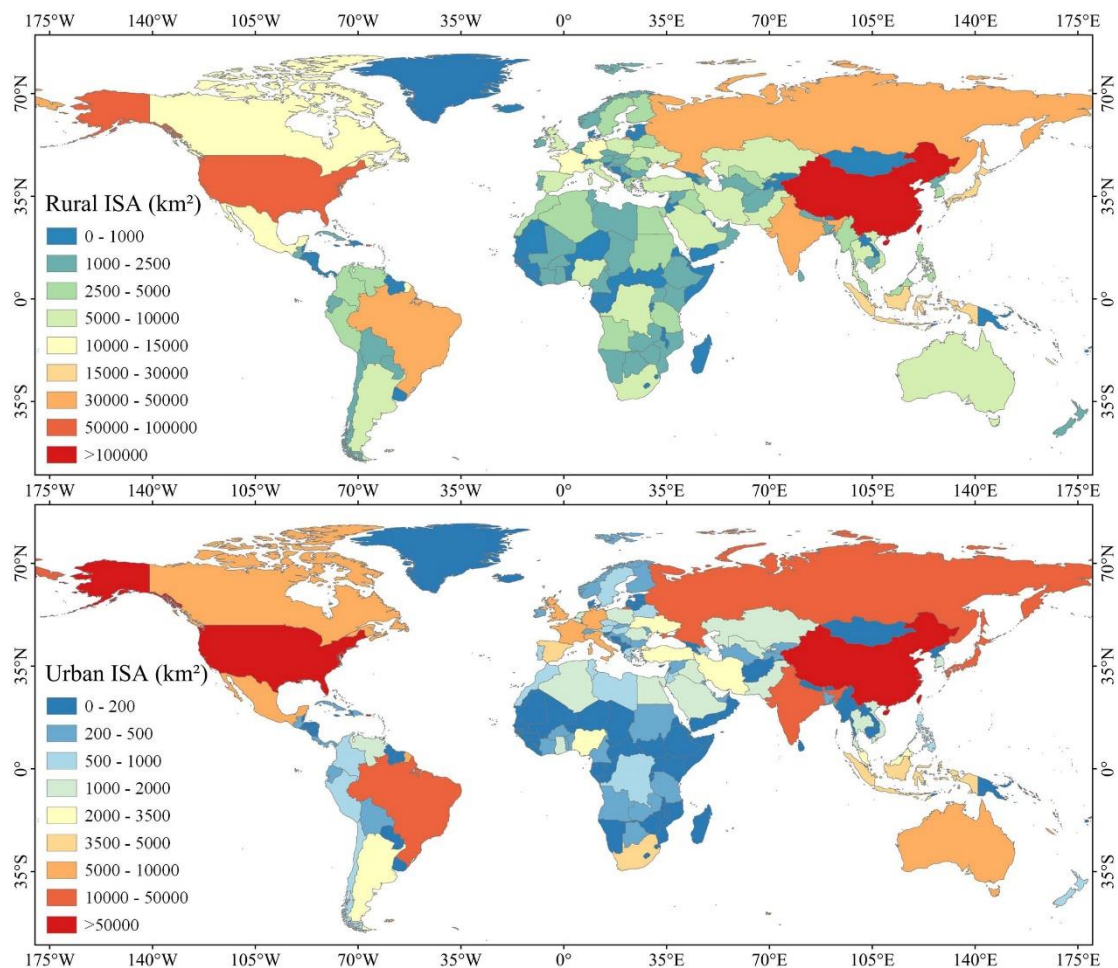
Figure 9. Urban and rural ISA at the country scale based in GISA-10m.

Toyama   Detroit   Chengdu   Riyadh
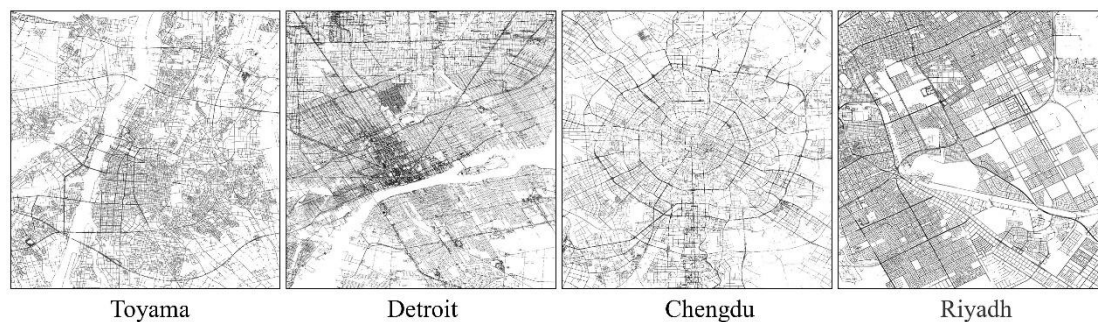
Figure 10. Examples of road area derived from GISA-10m and OSM in the Toyama (Japan), Detroit (US), Chengdu (China), and Riyadh (Saudi Arabia).

405

4.2.2 Global road area

Roads are major anthropic footprints, we attempted to analyse the global road area based on GISA-10m, by courtesy of its high spatial resolution. Firstly, the road networks were extracted from OSM, and then, the ISA regions in the GISA 10-m
410 within a 10-m buffer of the road networks were identified as the road areas (Fig. 10). Results showed that 82.84% of the global road areas located in Asia (30.74%), North America (27.17%) and Europe (24.92%), while the remaining 17.16% was owned by South America (8.26%), Africa (7.47%) and Oceania (1.44%). Although Asia exceeded the other continents regarding ISA and rural road area, it possessed less urban road area than North America. China and US had the largest road area, together accounting for 29% of the global total, which were followed by Brazil, Japan, Russia, Germany, India, France,
415 Indonesia, and Mexico. The top ten countries owned more than half of global roads. The global road area accounted for 14.18% of the global ISA, and rural road area was 1.5 times larger than urban (Table 7). However, it should be noted that these estimates might be biased owing to the incompleteness of the OSM data. In addition, narrow roads might be partly detected or missed due to the limitation of spatial resolution.

Table 7. Statistics of road network derived from GISA-10m and OSM in the six continents.

Road	Europe	Africa	S. America	Oceania	N. America	Asia	Globe
Total (10^4km^2)	3.51 (24.92%)	1.05 (7.47%)	1.16 (8.26%)	0.20 (1.44%)	3.83 (27.17%)	4.34 (30.74%)	14.10 (100%)
Rural (10^4km^2)	2.27 (26.88%)	0.71 (8.43%)	0.75 (8.88%)	0.11 (1.26%)	1.84 (21.73%)	2.77 (32.82%)	8.45 (100%)
Urban (10^4km^2)	1.24 (21.99%)	0.34 (6.03%)	0.42 (7.34%)	0.10 (1.70%)	2.00 (35.29%)	1.56 (27.65%)	5.66 (100%)
Rural/Urban	1.82	2.09	1.81	1.10	0.92	1.77	1.49

420 ## 5 Discussions

5.1 Inter-comparison with existing datasets

To further validate the performance of GISA-10m, we compared it with a series of existing state-of-the-art global datasets, including three 10-m datasets (i.e. WSF2015, GHSL2018, FROM_GLC10) and four 30-m datasets (i.e. GLCFCS, GAUD, GAIA, and GISA). The spatial agreements over urban and rural regions were estimated by the linear fitting of ISA fraction.
425 Considering their difference of spatial resolutions, the ISA fraction was calculated within the 0.05° spatial grid.
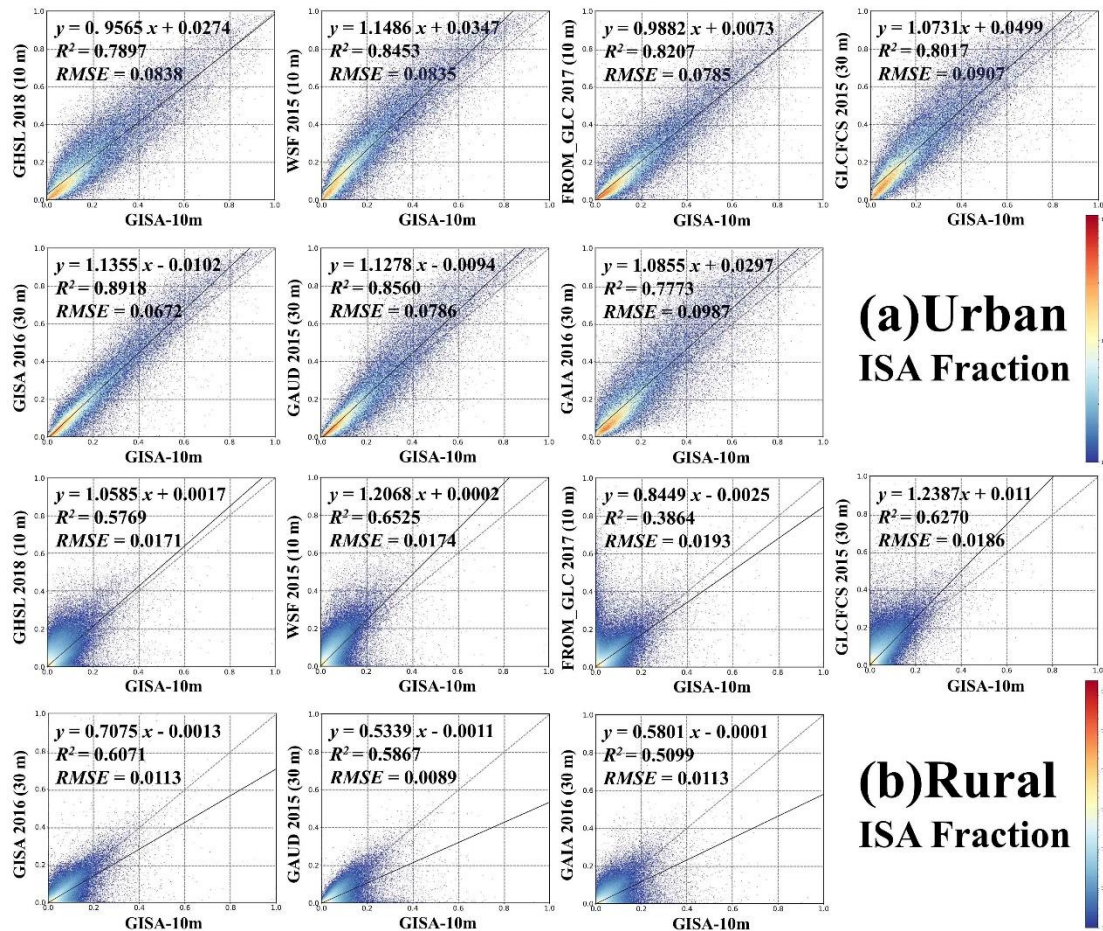
Figure 11. Scatterplots of (a) urban and (b) rural ISA fraction between GISA-10m with GHSL, WSF, FROM_GLC10, GLCFCS, GAUD, GAIA, GISA, respectively. ISA fraction was calculated within a 0.05° by 0.05° spatial grid.

In general, GISA-10m exhibited high agreement ($0.777 < R^2 < 0.892$) with these existing datasets over urban regions. In the

430 case of GHSL2018 and FROM_GLC10, their fitted lines with GISA-10m were closer to the 1:1 line in the high fraction

regions (Fig. 11a). As shown in the Fig.12, GHSL2018 and GISA-10m were generally similar in the dense urban areas (e.g.

urban cores in Fig.12), but GHSL2018 tended to overestimate ISA in the low-density residential areas (Fig.12c). The fitted

lines for GLCFCS and WSF2015 were above the diagonal (slope greater than 1 and intercept greater than 0) in both high and

low ISA fraction regions, possibly owing to their overestimations. For instance, in the case of Cairo (Fig. 12b), WSF2015

435 showed significant overestimations but other datasets better depicted the residential areas. According to Marconcini et al.,

(2020), the overestimations of the WSF2015 may be related to the employment of the coefficient of variation (COV), which

reduced the omissions in the rural regions but at the same time led to overestimations of ISA extent. The fitted lines for the

three 30-m datasets (i.e. GISA, GAIA, GAUD) were all above the diagonal (Fig. 11a), suggesting that they detected more

urban ISA than GISA-10 m. However, in the 30-m dataset, vegetation alongside roads or buildings was often identified as

440 ISA due to the issue of mixed pixels (Gong et al., 2020b). From this perspective, the results of GISA-10m seem more

reliable due to its high spatial resolution. For instance, in the case of Johannesburg and Los Angeles (Figs. 12c&d), GAIA and GAUD exhibited false alarms in both residential and industrial areas, but these errors were significantly reduced in GISA-10m due to the better discrimination ability of 10-m Sentinel data.
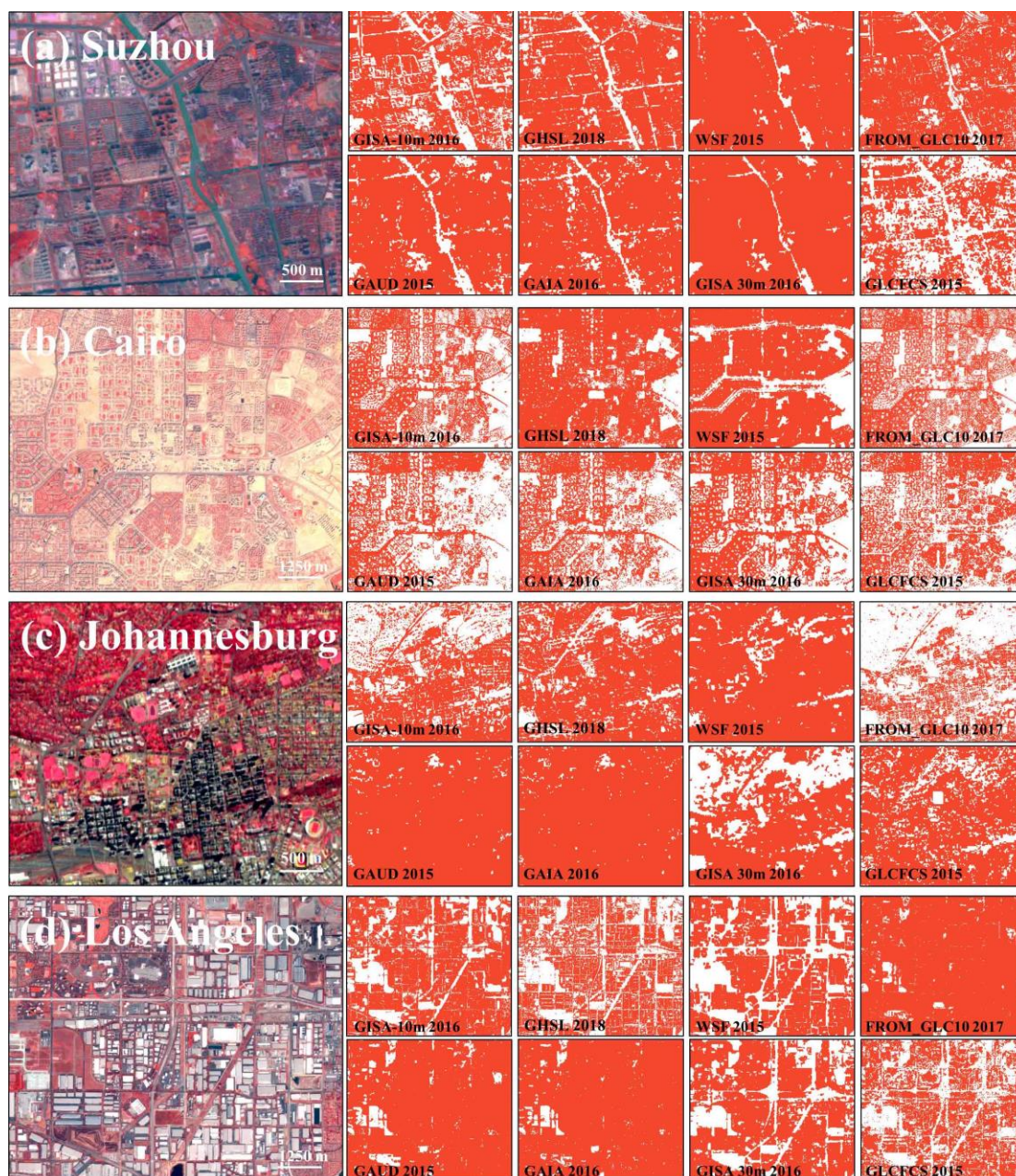
445 **Figure 12. Comparison of the GISA-10m and seven datasets over urban regions in (a) Suzhou, China; (b) Cairo, Egypt; (c) Johannesburg, South Africa; (d) Los Angeles, the United States. The Sentinel-2 images were composited in the false-color combination (R: NIR, G: Red, B: Green).**

23

On the other hand, the agreement between GISA-10m and existing datasets was slightly lower in rural regions ($0.5099 < R^2 < 0.6525$). The fitted slopes between three 30-m datasets (i.e. GISA, GAIA, GAUD) and GISA-10m in rural regions were all less than one. This phenomenon can be attributed to the finer spatial resolution of GISA-10m, which detected more rural ISA than the 30-m datasets (Figs. 13b&d). As to GLCFCS and WSF2015, they possessed more rural ISA than GISA-10m (Fig. 11b), which may be attributed their overestimations. For example, in Figs. 13a&c, GLCFCS and WSF2015 failed to identify the vegetation in the village. FROM_GLC10 seemed more consistent with GISA-10m (see the sample of US, Fig. 13d), but it tended to underestimate the rural ISA (see Figs. 13a-c). GHSL2018 and GISA-10m showed high agreement in the rural regions. However, GHSL2018 aimed to outline human settlements while GISA-10m focused on artificial ISA (including buildings, parking lot, roads).
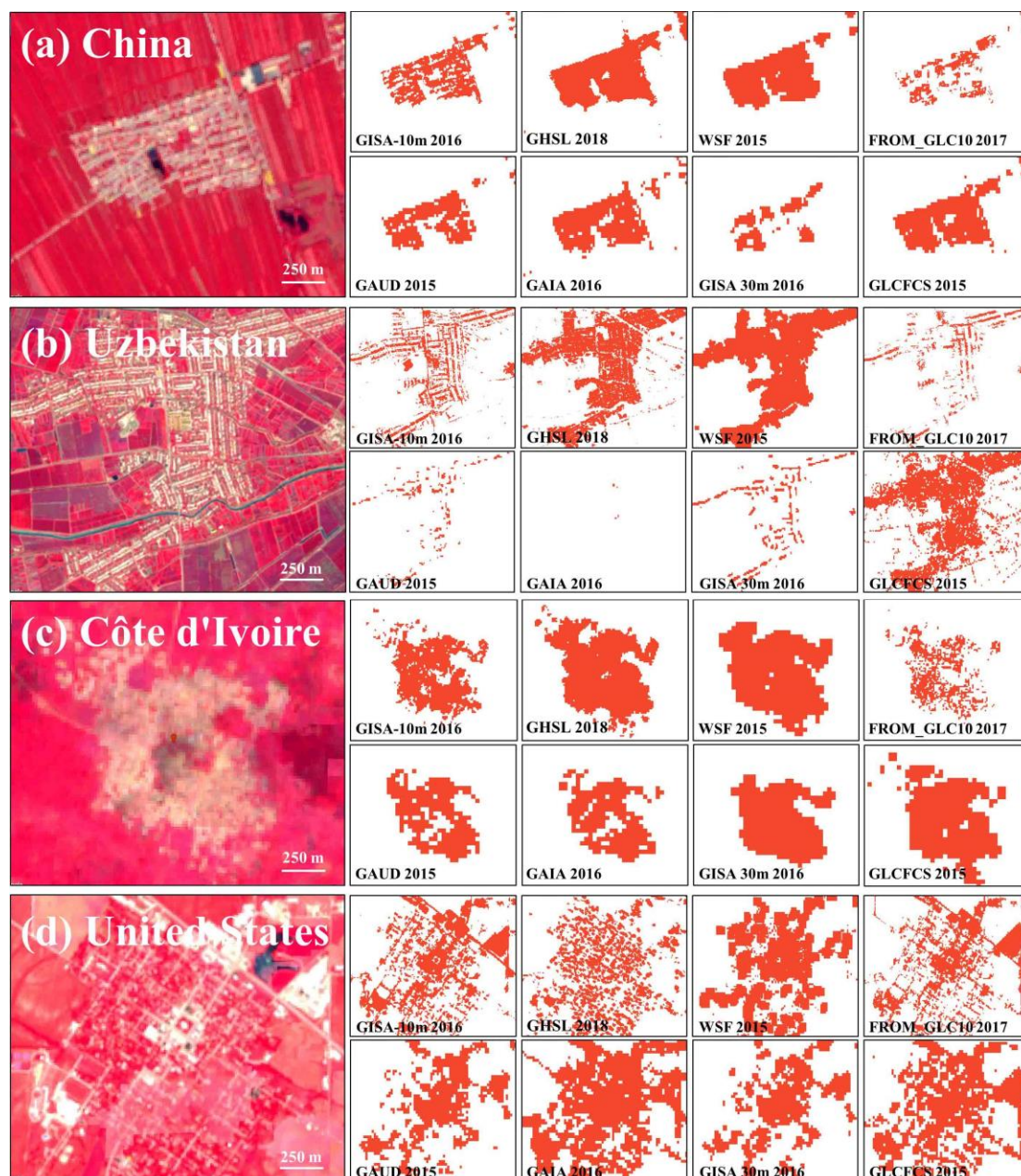
Figure 13. Comparison of the GISA-10m and seven datasets over rural regions in (a) China (126.348044° E, 45.269079° N), (b) Uzbekistan (60.573313° E, 41.461425° N), (c) Côte d'Ivoire (5.853317° W, 6.820244° N), (d) the United States (90.210747° W, 39.950221° N). The illustration is of Sentinel-2 images with false-color combination (R: NIR, G: Red, B: Green) to enhance the ISA.

460

The differences between GHSL2018, WSF2015 and GISA-10m were further analysed by taking Beijing and Washington as examples. In Fig. 14, the overlapping parts between these datasets were marked in different colors, and the regions where the three datasets all agreed were shown in gray. In both examples, WSF2015 and GHSL2018 tended to overestimate the ISA

extent (Fig. 14b). They wrongly identified vegetation as ISA in the low-density residential areas (Fig. 14h). In particular,

465 GHSL2018 successfully detected roads in Beijing but failed in Washington (see the color of purple in Fig. 14). This may be related to the fact that GHSL2018 used different sources of training samples in different regions (Corbane et al., 2021). Although WSF2015 generally obtained similar results with GISA-10m, its detected roads may stem from the overestimation of building boundaries (Marconcini et al., 2020). For instance, WSF2015 ignored the airport runways in the example of Beijing (Fig. 14d). In the case of Washington, WSF2015 was less capable of delineating scattered buildings than GISA-10m

470 and GHSL2018 (Fig. 14f), possibly because it also incorporated the 30-m Landsat data in the ISA detection. It should be mentioned that GHSL2018 estimated the probability of human settlement, and hence, different thresholds could yield different results. Small thresholds were suitable for capturing scattered settlements but could result in false alarms. In this study, we chose 0.2 as the threshold, as suggested by Corbane et al., (2021).
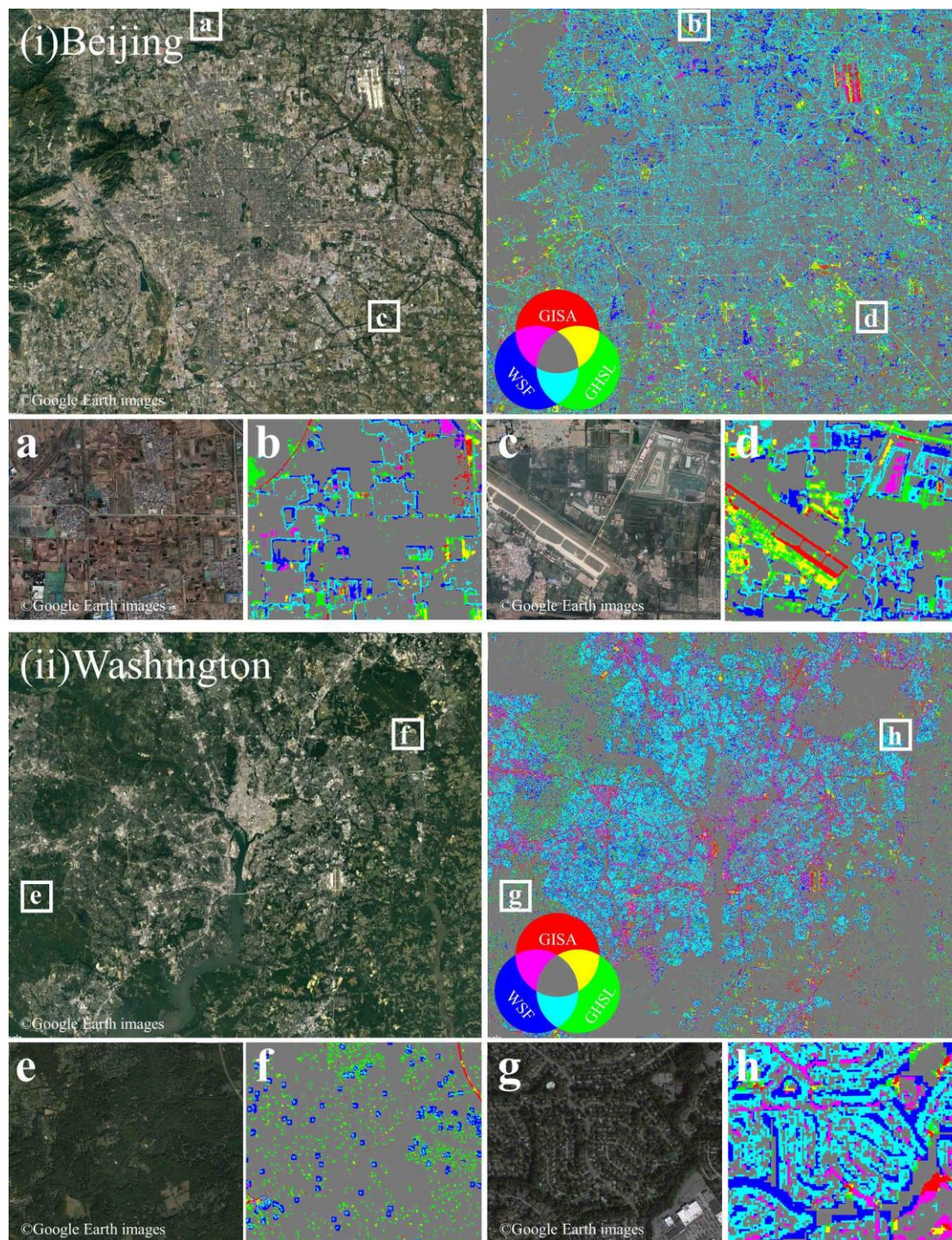
Figure 14. The illustration of WSF2015, GHSL2018 and GISA-10m in (i) Beijing and (ii) Washington. Regions where three datasets all agreed were shown in gray.

Earth System
Science
Data
Open Access
Discussions

5.2 Importance of multi-source features

In this paper, we proposed a global ISA mapping method that incorporated spectral, SAR, and temporal information extracted from multi-source Sentinel data. To illustrate the importance of multi-source features in the global ISA mapping,

480 we selected 30 hexagons in terms of the global urban ecoregions (Schneider et al., 2010). Urban ecoregions were defined with reference to biomes, urban landscapes, and economic levels. In each ecoregion, we randomly selected two grids, with their population greater or less than 5 million, respectively (Fig. S1). The "snow and ice" ecoregion was not considered. Feature contribution estimated by RF classifier was employed to analyze the relative importance of multi-source features (Pflugmacher et al., 2014; Zhang et al., 2020a). Different color schemes in Fig. 15 indicated different types of features. For

485 instance, the color of blue denoted SAR features while green represented the spectral indices. The results indicated that the feature importance varied in different regions. For example, SAR features were more effective in the temperate grassland of Middle East and Asia (53N_75E and 50N_39E), while phenological features had more influence in the deciduous forest of Siberia (65N_125E). In particular, SAR features played a more important role in the more populated regions, e.g. in temperate forest of North America and Europe as well as temperate grassland of the Middle East and Asia (Fig. 15).
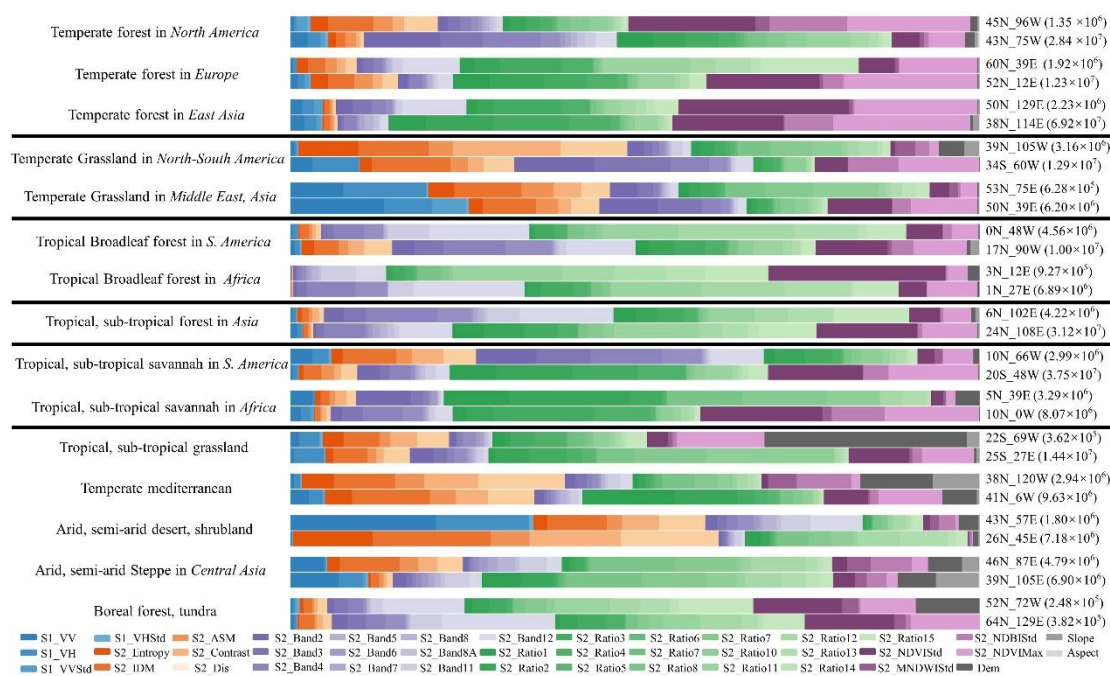

490

Figure 15. Relative importance of multi-source features in the 30 randomly selected grids located in different urban ecoregion. The labels on the right denote grid ID and total population. The Dis, IDM and ASM represents the dissimilarity, angular second moment and inverse difference moment, respectively.

It is worth noting that although high-rise ISA (e.g. buildings) tended to have higher radar backscatters, the importance of

495 SAR features was not always the highest. For example, in the hexagon of central US (45N_96W), SAR features played a less significant role than temporal metrics. In contrast, the spectral indices and phenological information were more effective in

this region. For example, as shown in Fig. 16 (red squares), in the residential area, the buildings were often surrounded by dense shrub, which may shrink the double bounce scattering. Therefore, spectral and phenological features had higher importance since they can better distinguish vegetation from non-vegetation. A similar situation occurred in a desert area 500 (26N_45E), where SAR features could not distinguish well ISA from NISA due to the complex topography of mountains. In this case, spectral indices and textures were more effective (Fig. 15). However, SAR features were still very important for global ISA mapping, especially for identifying rural buildings (Zhang et al., 2020a). Therefore, in this study, we used multi-source features and hexagon-based adaptive random forest models to ensure that the most suitable features were chosen for different regions.
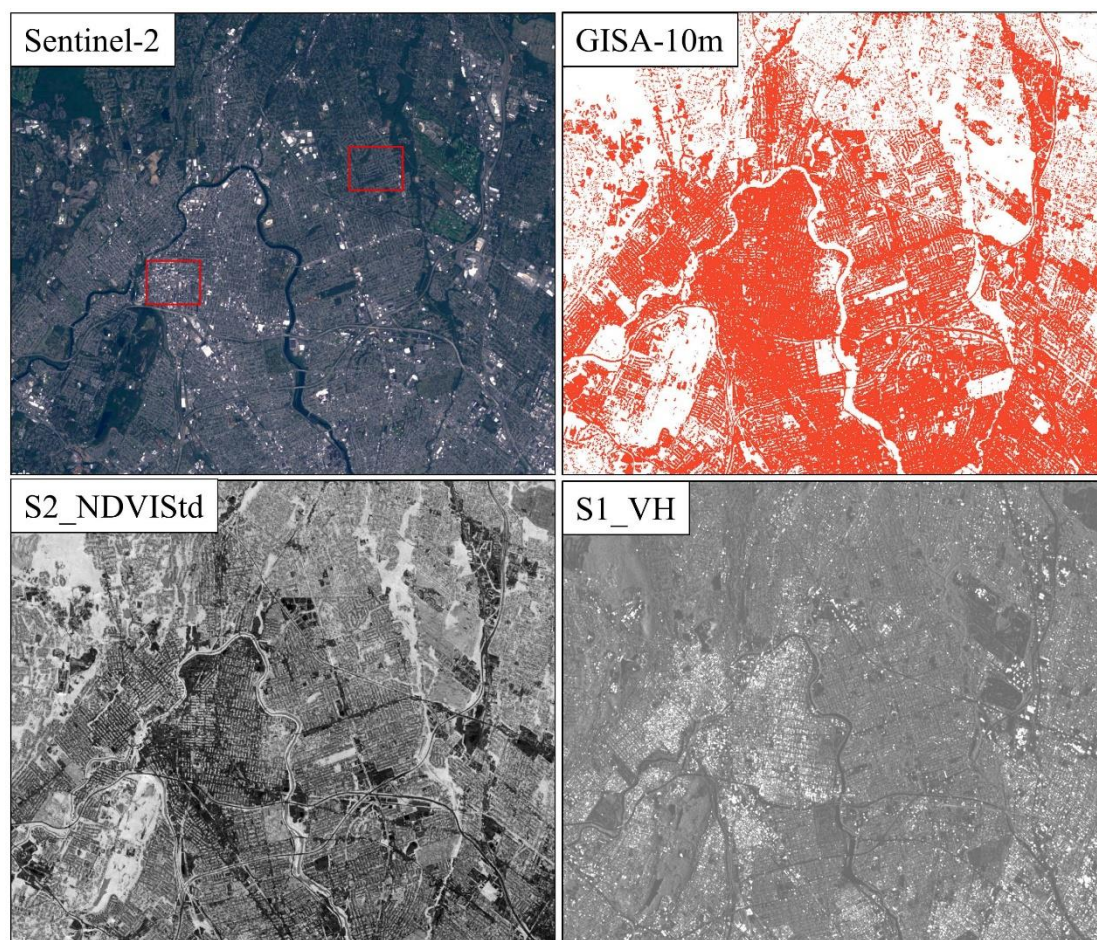
505

Figure 16. Example of Sentinel-1 VH backscatter, standard deviation of NDVI from Sentinel-2 (S2_NDVIStd), Sentinel-2 true color composite and GISA-10m in Paterson, New Jersey, the United States.

5.3 Impact of training sample size

Based on aforementioned randomly selected 30 hexagons in different urban ecoregions, we investigated the relationship 510 between the training sample size and the accuracy (Fig. S1). For each hexagon, we fixed the number of NISA samples to

30,000 and changed the number of ISA$_{RS}$ and ISA$_{OSM}$ samples. Specifically, we first randomly selected 1,000 ISA$_{RS}$, 1,000 ISA$_{OSM}$ and 2,000 NISA samples from the candidate pool (see Section 3.1.1) as the test samples and used the remaining ones for the training. We randomly selected 50 ISA$_{RS}$ and 50 ISA$_{OSM}$ as the initial training samples, and subsequently, in an iterative manner, 400 ISA$_{RS}$ and ISA$_{OSM}$ samples were randomly selected from the pool and added to the training samples to train the RF classifier. It can be observed that all the hexagons reached saturation with 2,500 ISA$_{RS}$ and ISA$_{OSM}$ samples (Fig. 17). Therefore, in this research, we set the number of ISA$_{RS}$, ISA$_{OSM}$, and NISA samples to 2,500, 2,500 and 30,000, respectively.
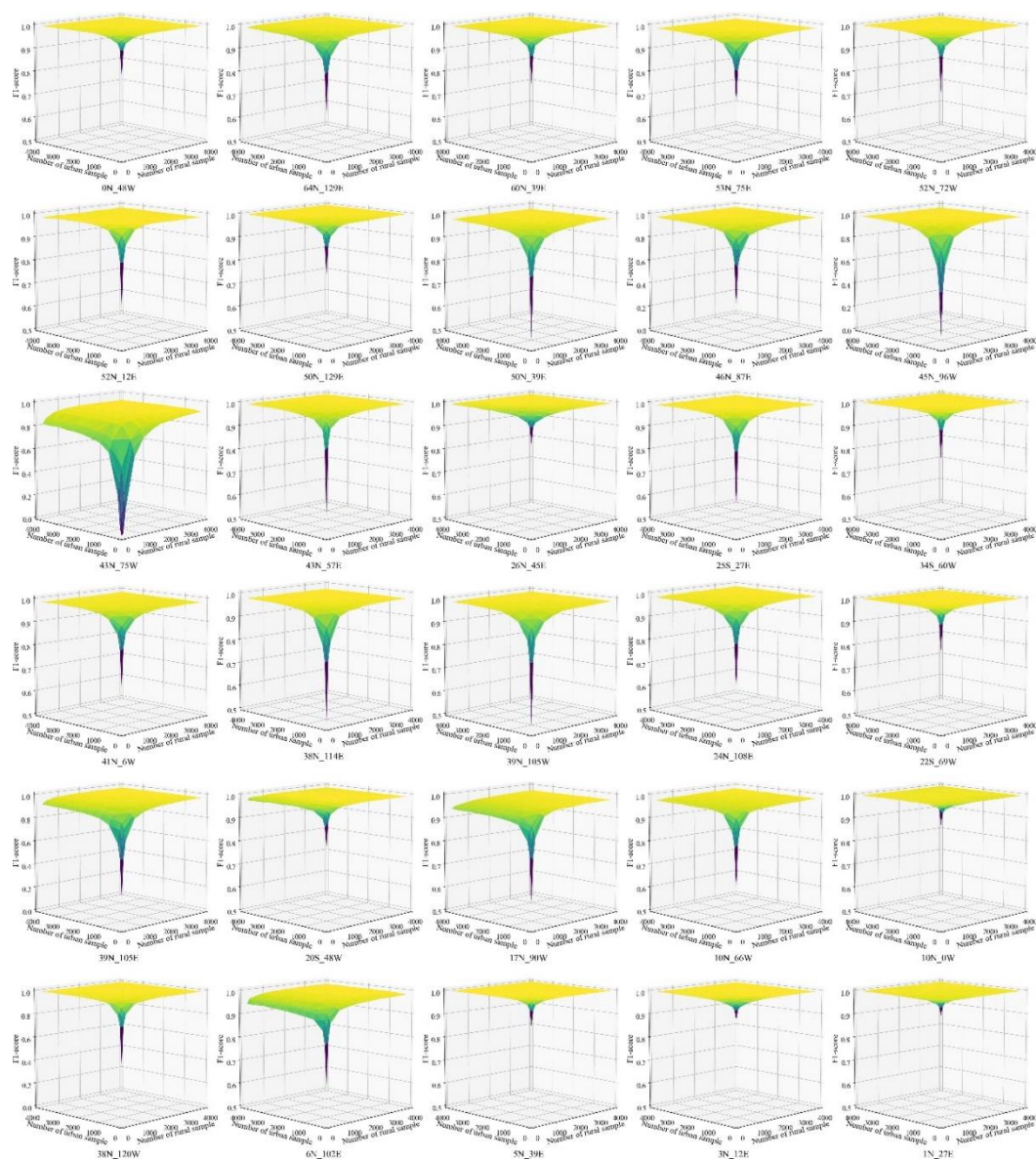
Figure 17. The F-Score as a function of ISA$_{RS}$ and ISA$_{OSM}$ samples in the randomly selected 30 global grids.

5.4 Advantages of locally adaptive RF classification

520

We used two hexagons located in China (CHN) and Saudi Arabia (SA) to demonstrate the advantages of adaptive random forest classification. Although China and Saudi Arabia are both located in Asia, their urban landscapes and architecture styles are significantly different due to their difference in climate, environment, and culture. In this section, we migrated the training samples from one hexagon to classify the other one. For example, training samples collected in the SA was used to

525 classify the hexagon of China. The accuracy of each hexagon was evaluated by the visually-interpreted samples inside it. It was found that the OA decreased by 34% when the SA samples was applied to CHN (written as SA-to-CHN). Similarly, the OA was substantially reduced by 23% by the transfer of CHN-to-SA. Furthermore, we found that local samples always outperformed the migrated ones (see Table 8), which verified the necessity of local and adaptive classification strategies in the global ISA mapping. Besides, the locally adaptive model is more sensitive to the sample quality compared to the global

530 model (Radoux et al., 2014), which further showed the necessity and effectiveness of the local classification strategy.

Table 8. Results of quantitative accuracy assessment for China (CHN) and Saudi Arabia (SA) based on local and transferred samples. OA denotes the overall accuracy.

	Saudi Arabia				China			
	OA (%)	Kappa	F-Score of ISA (%)	F-Score of NISA (%)	OA (%)	Kappa	F-Score of ISA (%)	F-Score of NISA (%)
ISA_SA & NISA_SA	**93.00**	**0.8599**	**92.39**	**93.95**	79.50	0.5915	77.60	81.86
ISA_SA & NISA_CN	53.00	0.7253	65.44	26.77	55.00	0.5233	4.35	70.59
ISA_CN & NISA_SA	70.50	0.8396	53.23	78.55	48.00	0.6251	63.38	10.53
ISA_CN & NISA_CN	50.50	0.0846	64.77	16.95	**89.00**	**0.7778**	**86.90**	**91.30**

5.5 Influence of the sources of training samples

In this section, the effects of the training sample sources, i.e., from remote sensing dataset (ISA_{RS}) and the OSM (ISA_{OSM}),

535 were investigated. Various combinations of the ISA_{RS} and ISA_{OSM} samples were tested at the global scale (Table 9). In general, it can be found that using both sources yielded the most accurate results, which showed the effectiveness and necessity of incorporation of training samples from remote sensing and crowdsourcing OSM. By further checking the UA and PA of ISA, one can see that using both sample sources significantly improved the PA and reduced the ISA omissions, since the combination of ISA_{RS} and ISA_{OSM} strengthened the diversity of the training samples. Similarly, it was also found

540 that the multi-source samples significantly raised the PA of NISA and lowered its commission error. Although the quality and consistency of OSM data may affect the performance of GISA-10m (Fan et al., 2014; Zacharopoulou et al., 2021), global ISA mapping using only ISA_{OSM} showed relatively consistent accuracy across continents (Fig.S3). This can be attributed to rule-based method we implemented that improved the reliability and spatial consistency of ISA_{OSM}. In addition, the collaboration of ISA_{OSM} improved the overall accuracy of global ISA mapping by 3% (Table 9), indicating the feasibility

545 of OSM data in enhancing performance of global ISA mapping after a set of refinements.

Table 9. Results of global accuracy assessment for ISA$_{RS}$ and ISA$_{OSM}$ sample. OA denotes the overall accuracy, while PA and UA indicate the user's accuracy and the producer's accuracy, respectively.

Source of training sample	OA (%)	Kappa	F-Score of ISA (%)	F-Score of NISA (%)	UA of ISA (%)	PA of ISA (%)	UA of NISA (%)	PA of NISA (%)
NISA+ISA$_{RS}$+ISA$_{OSM}$	**86.06**	**0.7165**	**83.65**	**88.55**	86.13	**81.30**	**86.01**	91.25
NISA+ISA$_{RS}$	80.24	0.5871	73.85	84.63	**88.16**	63.54	76.73	**94.35**
NISA+ISA$_{OSM}$	82.99	0.6500	78.96	86.34	86.24	72.81	81.17	92.23

6 Data availability

The GISA-10m product generated in this study is available in the public domain at http://doi.org/10.5281/zenodo.5791855

550 (Huang et al, 2021). Sentinel data were acquired from the Google Earth Engine (available at code.earthengine.google.com, last access: 6 August 2021). GHSL was provided by the Joint Research Centre at European Commission (available at https://ghsl.jrc.ec.europa.eu/datasets.php, last access: 19 December 2021). WSF was provided by the German Aerospace Center (https://doi.org/10.6084/m9.figshare.c.4712852, Marconcini et al., 2020).The GlobeLand30 and GAUD were downloaded from the website of the National Geomatics Center of China (available at http://www.globallandcover.com/, last

555 access: 6 August 2021) and Sun Yat-sen University (available at https://doi.org/10.6084/m9.figshare.11513178.v1, Liu et al., 2020b). FROM_GLC10 and GAIA were assessed from the Tsinghua University (available at http://data.ess.tsinghua.edu.cn, last access: 6 August 2021). The GISA was provided by the Institute of Remote Sensing Information Processing at Wuhan University (available at https://zenodo.org/record/5136330, Huang et al., 2021a). GLCFCS was provided by Aerospace Information Research Institute at Chinese Academy of Sciences (available at https://zenodo.org/record/4280923, Zhang et al.,

560 2020b). The planet files were download from the website of OpenStreetMap (available at https://planet.openstreetmap.org, last access: 19 December 2021).

7 Conclusion

In this study, we proposed a global ISA mapping method and produced the 10-m global ISA dataset (GISA-10m). To our knowledge, this is the first global 10-m ISA map based on Sentienl-1 and 2 data. To this end, a global training sample

565 generation method was proposed based on a series of temporal, spatial, spectral, and geometrical rules and 58 million training samples were generated from the existing global ISA datasets and the social sensing data (i.e., OSM). On the basis of the 2.7 million Sentinel images available in the Google Earth Engine (GEE), multi-source features were constructed including spectral, texture, SAR, and temporal metrics. The global terrestrial surface was divided with hexagons, and the results were obtained by a series of RF classifiers. In particular, the mapping was conducted adaptively for each hexagon, by

570 considering the difficulty and diversity for the global ISA detection. The overall accuracy of GISA-10m exceeded 86% based on a set of independent test samples. The inter-comparison between different global ISA datasets showed the

superiority of our results. Based on GISA-10m, the ISA distribution at the global, continental, and country levels was discussed and compared. In addition, the global ISA distribution was compared between rural and urban. In particular, for the first time, by courtesy of the high spatial resolution, the global road ISA was further identified and its distribution was discussed.

GISA-10m can be used for global climate change studies and urban planning. Our proposed rule-based sample generation method can also be applied for global mapping of other land cover categories. For example, millions of cropland and forest tags in the OSM can facilitate global high-resolution cropland and forest mapping. The ISA mapping method via multi-source geospatial data presented in this paper can also be improved by incorporating additional data sources, such as building footprints from Microsoft and Facebook (Corbane et al., 2021). In the future, we plan to extend the temporal coverage of GISA-10m and reveal the global ISA dynamics at the 10-m resolution.

Author contributions. XH conceived the study. XH, JY, WW and ZL designed and implemented the methodology. JY prepared original draft and XH revised it.

Competing interests. The authors declare that they have no conflict of interest.

References

Ban, Y., Jacob, A. and Gamba, P.: Spaceborne SAR data for global urban mapping at 30m resolution using a robust urban extractor, ISPRS J. Photogramm. Remote Sens., 103, 28–37, doi:https://doi.org/10.1016/j.isprsjprs.2014.08.004, 2015.

Bauer, E. and Kohavi, R.: Empirical comparison of voting classification algorithms: bagging, boosting, and variants, Mach. Learn., 36(1), 105–139, doi:10.1023/a:1007515423169, 1999.

Birch, C. P. D., Oom, S. P. and Beecham, J. A.: Rectangular and hexagonal grids used for observation, experiment and simulation in ecology, Ecol. Modell., 206(3), 347–359, doi:https://doi.org/10.1016/j.ecolmodel.2007.03.041, 2007.

605   Breiman, L.: Random forests, Mach. Learn., 45(1), 5–32, doi:10.1023/A:1010933404324, 2001.

Chen, J., Chen, J., Liao, A., Cao, X., Chen, L., Chen, X., He, C., Han, G., Peng, S., Lu, M., Zhang, W., Tong, X. and Mills, J.: Global land cover mapping at 30 m resolution: A POK-based operational approach, ISPRS J. Photogramm. Remote Sens., 103, 7–27, doi:10.1016/j.isprsjprs.2014.09.002, 2015.

Clausi, D. A.: An analysis of co-occurrence texture statistics as a function of grey level quantization, Can. J. Remote Sens.,
610   28(1), 45–62, doi:10.5589/m02-004, 2002.

Conners, R. W., Trivedi, M. M. and Harlow, C. A.: Segmentation of a high-resolution urban scene using texture operators, Comput. Vision, Graph. Image Process., 25(3), 273–310, doi:https://doi.org/10.1016/0734-189X(84)90197-X, 1984.

Corbane, C., Syrris, V., Sabo, F., Politis, P., Melchiorri, M., Pesaresi, M., Soille, P. and Kemper, T.: Convolutional neural networks for global human settlements mapping from Sentinel-2 satellite imagery, Neural Comput. Appl., 33(12), 6697–
615   6720, doi:10.1007/s00521-020-05449-7, 2021.

Dewan, A. M. and Yamaguchi, Y.: Land use and land cover change in Greater Dhaka, Bangladesh: Using remote sensing to promote sustainable urbanization, Appl. Geogr., 29(3), 390–401, doi:10.1016/j.apgeog.2008.12.005, 2009.

Drusch, M., Del Bello, U., Carlier, S., Colin, O., Fernandez, V., Gascon, F., Hoersch, B., Isola, C., Laberinti, P., Martimort, P., Meygret, A., Spoto, F., Sy, O., Marchese, F. and Bargellini, P.: Sentinel-2: ESA's Optical High-Resolution Mission for
620   GMES Operational Services, Remote Sens. Environ., 120, 25–36, doi:https://doi.org/10.1016/j.rse.2011.11.026, 2012.

Fan, H., Zipf, A., Fu, Q. and Neis, P.: Quality assessment for building footprints data on OpenStreetMap, Int. J. Geogr. Inf. Sci., 28(4), 700–719, doi:10.1080/13658816.2013.867495, 2014.

Fonte, C. C., Patriarca, J., Jesus, I. and Duarte, D.: Automatic Extraction and Filtering of OpenStreetMap Data to Generate Training Datasets for Land Use Land Cover Classification, Remote Sens. , 12(20), doi:10.3390/rs12203428, 2020.

625   Foody, G. M.: Sample size determination for image classification accuracy assessment and comparison, Int. J. Remote Sens., 30(20), 5273–5291, doi:10.1080/01431160903130937, 2009.

Foody, G. M. and Arora, M. K.: An evaluation of some factors affecting the accuracy of classification by an artificial neural network, Int. J. Remote Sens., 18(4), 799–810, doi:10.1080/014311697218764, 1997.

Friedl, M. A., Sulla-Menashe, D., Tan, B., Schneider, A., Ramankutty, N., Sibley, A. and Huang, X.: MODIS Collection 5
630   global land cover: Algorithm refinements and characterization of new datasets, Remote Sens. Environ., 114(1), doi:10.1016/j.rse.2009.08.016, 2010.

Gamba, P. and Lisini, G.: Fast and Efficient Urban Extent Extraction Using ASAR Wide Swath Mode Data, IEEE J. Sel. Top. Appl. Earth Obs. Remote Sens., 6(5), 2184–2195, doi:10.1109/JSTARS.2012.2235410, 2013.

Gislason, P. O., Benediktsson, J. A. and Sveinsson, J. R.: Random Forests for land cover classification, Pattern Recognit.
635   Lett., 27(4), 294–300, doi:https://doi.org/10.1016/j.patrec.2005.08.011, 2006.

Goetz, M.: Towards generating highly detailed 3D CityGML models from OpenStreetMap, Int. J. Geogr. Inf. Sci., 27(5), 845–865, doi:10.1080/13658816.2012.721552, 2013.

Goetz, S. J., Wright, R. K., Smith, A. J., Zinecker, E. and Schaub, E.: IKONOS imagery for resource management: Tree cover, impervious surfaces, and riparian buffer analyses in the mid-Atlantic region, Remote Sens. Environ., 88(1–2), 195–
640   208, doi:10.1016/j.rse.2003.07.010, 2003.

Goldblatt, R., You, W., Hanson, G. and Khandelwal, A. K.: Detecting the Boundaries of Urban Areas in India: A Dataset for Pixel-Based Image Classification in Google Earth Engine, Remote Sens. , 8(8), doi:10.3390/rs8080634, 2016.

Goldblatt, R., Stuhlmacher, M. F., Tellman, B., Clinton, N., Hanson, G., Georgescu, M., Wang, C., Serrano-Candela, F., Khandelwal, A. K., Cheng, W.-H. and Balling, R. C.: Using Landsat and nighttime lights for supervised pixel-based image
645   classification of urban land cover, Remote Sens. Environ., 205, 253–275, doi:https://doi.org/10.1016/j.rse.2017.11.026, 2018.

Goldewijk, K. K.: Estimating global land use change over the past 300 years: The HYDE database, Global Biogeochem. Cycles, 15(2), 417–433, doi:10.1029/1999GB001232, 2001.

Gong, J., Liu, C. and Huang, X.: Advances in urban information extraction from high-resolution remote sensing imagery, Sci. China Earth Sci., 63(4), 463–475, doi:10.1007/s11430-019-9547-x, 2020a.

650   Gong, P., Liu, H., Zhang, M., Li, C., Wang, J., Huang, H., Clinton, N., Ji, L., Li, W., Bai, Y., Chen, B., Xu, B., Zhu, Z., Yuan, C., Ping Suen, H., Guo, J., Xu, N., Li, W., Zhao, Y., Yang, J., Yu, C., Wang, X., Fu, H., Yu, L., Dronova, I., Hui, F., Cheng, X., Shi, X., Xiao, F., Liu, Q. and Song, L.: Stable classification with limited sample: transferring a 30-m resolution sample set collected in 2015 to mapping 10-m resolution global land cover in 2017, Sci. Bull., 64(6), 370–373, doi:10.1016/j.scib.2019.03.002, 2019.

655   Gong, P., Li, X., Wang, J., Bai, Y., Chen, B., Hu, T., Liu, X., Xu, B., Yang, J., Zhang, W. and Zhou, Y.: Annual maps of global artificial impervious area (GAIA) between 1985 and 2018, Remote Sens. Environ., 236, 111510, doi:10.1016/j.rse.2019.111510, 2020b.

Goodchild, M. F.: Citizens as sensors: the world of volunteered geography, GeoJournal, 69(4), 211–221, doi:10.1007/s10708-007-9111-y, 2007.

660   Gorelick, N., Hancher, M., Dixon, M., Ilyushchenko, S., Thau, D. and Moore, R.: Google Earth Engine: Planetary-scale geospatial analysis for everyone, Remote Sens. Environ., 202, 18–27, doi:10.1016/j.rse.2017.06.031, 2017.

Haklay, M. and Weber, P.: OpenStreetMap: User-Generated Street Maps, IEEE Pervasive Comput., 7(4), 12–18, doi:10.1109/MPRV.2008.80, 2008.

Haralick, R. M., Shanmugam, K. and Dinstein, I.: Textural Features for Image Classification, IEEE Trans. Syst. Man.
665   Cybern., SMC-3(6), 610–621, doi:10.1109/TSMC.1973.4309314, 1973.

Herold, M., Latham, J. S., Di Gregorio, A. and Schmullius, C. C.: Evolving standards in land cover characterization, J. Land Use Sci., 1(2–4), 157–168, doi:10.1080/17474230601079316, 2006.

Homer, C., Huang, C., Yang, L., Wylie, B. and Coan, M.: Development of a 2001 National Land-Cover Database for the United States, Photogramm. Eng. Remote Sensing, 70(7), 829–840, doi:10.14358/PERS.70.7.829, 2004.

670   Huang, X. and Zhang, L.: An SVM Ensemble Approach Combining Spectral, Structural, and Semantic Features for the

Classification of High-Resolution Remotely Sensed Imagery, IEEE Trans. Geosci. Remote Sens., 51(1), 257–272,

doi:10.1109/TGRS.2012.2202912, 2013.

Huang, X., Li, J., Yang, J., Zhang, Z., Li, D., Liu, X., Xin, H., Jiayi, L., Jie, Y., Zhen, Z., Dongrui, L. and Xiaoping, L.: 30 m

global impervious surface area dynamics and urban expansion pattern observed by Landsat satellites: From 1972 to 2019,

675   Sci. CHINA Earth Sci., doi:10.1007/s11430-020-9797-9, 2021a.

Huang, X., Huang, J., Wen, D. and Li, J.: An updated MODIS global urban extent product (MGUP) from 2001 to 2018

based on an automated mapping approach, Int. J. Appl. Earth Obs. Geoinf., 95, 102255,

doi:https://doi.org/10.1016/j.jag.2020.102255, 2021b.

Huang, X., Yang J., Wang W. and Liu Z.: Mapping 10-m global impervious surface area (GISA-10m) using multi-source

680   geospatial data, Zenodo, https://doi.org/10.5281/ZENODO.5791855, 2021.

Ji, H., Li, X., Wei, X., Liu, W., Zhang, L. and Wang, L.: Mapping 10-m Resolution Rural Settlements Using Multi-Source

Remote Sensing Datasets with the Google Earth Engine Platform, Remote Sens. , 12(17), doi:10.3390/rs12172832, 2020.

Johnson, B. A. and Iizuka, K.: Integrating OpenStreetMap crowdsourced data and Landsat time-series imagery for rapid land

use/land cover (LULC) mapping: Case study of the Laguna de Bay area of the Philippines, Appl. Geogr., 67, 140–149,

685   doi:https://doi.org/10.1016/j.apgeog.2015.12.006, 2016.

Jokar Arsanjani, J., See, L. and Tayyebi, A.: Assessing the suitability of GlobeLand30 for mapping land cover in Germany,

Int. J. Digit. Earth, 9(9), 873–891, doi:10.1080/17538947.2016.1151956, 2016.

Leng, G., Tang, Q. and Rayburg, S.: Climate change impacts on meteorological, agricultural and hydrological droughts in

China, Glob. Planet. Change, 126, 23–34, doi:10.1016/j.gloplacha.2015.01.003, 2015.

690   Li, J., Gao, Y. and Huang, X.: The impact of urban agglomeration on ozone precursor conditions: A systematic investigation

across global agglomerations utilizing multi-source geospatial datasets, Sci. Total Environ., 704, 135458,

doi:10.1016/j.scitotenv.2019.135458, 2020a.

Li, X., Gong, P., Zhou, Y., Wang, J., Bai, Y., Chen, B., Hu, T., Xiao, Y., Xu, B., Yang, J., Liu, X., Cai, W., Huang, H., Wu,

T., Wang, X., Lin, P., Li, X., Chen, J., He, C., Li, X., Yu, L., Clinton, N. and Zhu, Z.: Mapping global urban boundaries

695   from the global artificial impervious area (GAIA) data, Environ. Res. Lett., 15(9), 94044, doi:10.1088/1748-9326/ab9be3,

2020b.

Lin, Y., Zhang, H., Lin, H., Gamba, P. E. and Liu, X.: Incorporating synthetic aperture radar and optical images to

investigate the annual dynamics of anthropogenic impervious surface at large scale, Remote Sens. Environ., 242, 111757,

doi:https://doi.org/10.1016/j.rse.2020.111757, 2020.

700   Liu, C., Huang, X., Zhu, Z., Chen, H., Tang, X. and Gong, J.: Automatic extraction of built-up area from ZY3 multi-view

satellite imagery: Analysis of 45 global cities, Remote Sens. Environ., 226, 51–73,

doi:https://doi.org/10.1016/j.rse.2019.03.033, 2019.

Earth System
Science Data

Open Access

Discussions

Liu, D., Chen, N., Zhang, X., Wang, C. and Du, W.: Annual large-scale urban land mapping based on Landsat time series in Google Earth Engine and OpenStreetMap data: A case study in the middle Yangtze River basin, ISPRS J. Photogramm.

705   Remote Sens., 159, 337–351, doi:https://doi.org/10.1016/j.isprsjprs.2019.11.021, 2020a.

Liu, X., Huang, Y., Xu, X., Li, X., Li, X., Ciais, P., Lin, P., Gong, K., Ziegler, A. D., Chen, A., Gong, P., Chen, J., Hu, G., Chen, Y., Wang, S., Wu, Q., Huang, K., Estes, L. and Zeng, Z.: High-spatiotemporal-resolution mapping of global urban change from 1985 to 2015, Nat. Sustain., 3(7), 564–570, doi:10.1038/s41893-020-0521-x, 2020b.

Marconcini, M., Metz-Marconcini, A., Üreyen, S., Palacios-Lopez, D., Hanke, W., Bachofer, F., Zeidler, J., Esch, T.,

710   Gorelick, N., Kakarla, A., Paganini, M. and Strano, E.: Outlining where humans live, the World Settlement Footprint 2015, Sci. Data, 7(1), 242, doi:10.1038/s41597-020-00580-5, 2020.

Olofsson, P., Foody, G. M., Herold, M., Stehman, S. V., Woodcock, C. E. and Wulder, M. A.: Good practices for estimating area and assessing accuracy of land change, Remote Sens. Environ., 148, 42–57, doi:10.1016/j.rse.2014.02.015, 2014.

Olson, D. M., Dinerstein, E., Wikramanayake, E. D., Burgess, N. D., Powell, G. V. N., Underwood, E. C., D'Amico, J. A.,

715   Itoua, I., Strand, H. E., Morrison, J. C., Loucks, C. J., Allnutt, T. F., Ricketts, T. H., Kura, Y., Lamoreux, J. F., Wettengel, W. W., Hedao, P. and Kassem, K. R.: Terrestrial ecoregions of the world: A new map of life on Earth, Bioscience, 51(11), 933–938, doi:10.1641/0006-3568(2001)051[0933:TEOTWA]2.0.CO;2, 2001.

Pflugmacher, D., Cohen, W. B., Kennedy, R. E. and Yang, Z.: Using Landsat-derived disturbance and recovery history and lidar to map forest biomass dynamics, Remote Sens. Environ., 151, 124–137, doi:https://doi.org/10.1016/j.rse.2013.05.033,

720   2014.

Puissant, A., Hirsch, J. and Weber, C.: The utility of texture analysis to improve per-pixel classification for high to very high spatial resolution imagery, Int. J. Remote Sens., 26(4), 733–745, doi:10.1080/01431160512331316838, 2005.

Qin, L., Wu, W., Tian, Y. and Xu, W.: LiDAR Filtering of Urban Areas With Region Growing Based on Moving-Window Weighted Iterative Least-Squares Fitting, IEEE Geosci. Remote Sens. Lett., 14(6), 841–845,

725   doi:10.1109/LGRS.2017.2682854, 2017.

Qin, L., Xu, W., Tian, Y., Chen, B. and Wang, S.: A River Channel Extraction Method for Urban Environments Based on Terrain Transition Lines, Water Resour. Res., 54(7), 4887–4900, doi:https://doi.org/10.1029/2018WR023095, 2018.

Radoux, J., Lamarche, C., Van Bogaert, E., Bontemps, S., Brockmann, C. and Defourny, P.: Automated Training Sample Extraction for Global Land Cover Mapping, Remote Sens, 6, 3966, doi:10.3390/rs6053965, 2014.

730   Richards, T., Gallego, J. and Achard, F.: Sampling for forest cover change assessment at the pan-tropical scale, Int. J. Remote Sens., 21(6–7), 1473–1490, doi:10.1080/014311600210272, 2000.

Rodriguez-Galiano, V. F., Chica-Olmo, M., Abarca-Hernandez, F., Atkinson, P. M. and Jeganathan, C.: Random Forest classification of Mediterranean land cover using multi-seasonal imagery and multi-seasonal texture, Remote Sens. Environ., 121, 93–107, doi:https://doi.org/10.1016/j.rse.2011.12.003, 2012.

735   Small, C., Pozzi, F. and Elvidge, C. D.: Spatial analysis of global urban extent from DMSP-OLS night lights, Remote Sens. Environ., 96(3), 277–291, doi:https://doi.org/10.1016/j.rse.2005.02.002, 2005.

Stehman, S. V: Impact of sample size allocation when using stratified random sampling to estimate accuracy and area of land-cover change, Remote Sens. Lett., 3(2), 111–120, doi:10.1080/01431161.2010.541950, 2012.

Stehman, S. V and Foody, G. M.: Key issues in rigorous accuracy assessment of land cover products, Remote Sens. Environ.,
740   231, 111199, doi:https://doi.org/10.1016/j.rse.2019.05.018, 2019.

Story, M. and Congalton, R.: Accuracy assessment: a user's perspective, Photogramm. Eng. Remote Sensing, 52, 397–399, 1986.

Tian, Y., Chen, H., Song, Q. and Zheng, K.: A Novel Index for Impervious Surface Area Mapping: Development and Validation, Remote Sens. , 10(10), doi:10.3390/rs10101521, 2018.

745   Tian, Y., Zhou, Q. and Fu, X.: An Analysis of the Evolution, Completeness and Spatial Patterns of OpenStreetMap Building Data in China, ISPRS Int. J. Geo-Information , 8(1), doi:10.3390/ijgi8010035, 2019.

Tucker, C. J.: Red and photographic infrared linear combinations for monitoring vegetation, Remote Sens. Environ., 8(2), 127–150, doi:10.1016/0034-4257(79)90013-0, 1979.

Turner, M. G.: Landscape ecology: the effect of pattern on process, Annu. Rev. Ecol. Syst. Vol. 20, 171–197,
750   doi:10.1146/annurev.es.20.110189.001131, 1989.

United Nations: Goal 11: Sustainable Cities and Communities - SDG Tracker, [online] Available from: https://sdg-tracker.org/cities (Accessed 25 April 2021), 2016.

United Nations: 2018 Revision of World Urbanization Prospects | Multimedia Library - United Nations Department of Economic and Social Affairs, [online] Available from: https://www.un.org/development/desa/publications/2018-revision-of-
755   world-urbanization-prospects.html (Accessed 25 April 2021), 2018.

Voss, P. R.: Demography as a Spatial Social Science, Popul. Res. Policy Rev., 26(5), 457–476, doi:10.1007/s11113-007-9047-4, 2007.

Wehmann, A. and Liu, D.: A spatial-temporal contextual Markovian kernel method for multi-temporal land cover mapping, ISPRS J. Photogramm. Remote Sens., 107, 77–89, doi:10.1016/j.isprsjprs.2015.04.009, 2015.

760   Weng, Q.: Remote sensing of impervious surfaces in the urban areas: Requirements, methods, and trends, Remote Sens. Environ., 117, 34–49, doi:https://doi.org/10.1016/j.rse.2011.02.030, 2012.

Wessels, K. J., Bergh, F. van den, Roy, D. P., Salmon, B. P., Steenkamp, K. C., MacAlister, B., Swanepoel, D. and Jewitt, D.: Rapid land cover map updates using change detection and robust random forest classifiers, Remote Sens., 8(11), 888, doi:10.3390/rs8110888, 2016.

765   Woodcock, C. E., Allen, R., Anderson, M., Belward, A., Bindschadler, R., Cohen, W., Gao, F., Goward, S. N., Helder, D., Helmer, E., Nemani, R., Oreopoulos, L., Schott, J., Thenkabail, P. S., Vermote, E. F., Vogelmann, J., Wulder, M. A. and Wynne, R.: Free access to landsat imagery, Science (80-.)., 320(5879), 1011, doi:10.1126/science.320.5879.1011a, 2008.

Wulder, M. A., Coops, N. C., Roy, D. P., White, J. C. and Hermosilla, T.: Land cover 2.0, Int. J. Remote Sens., 39(12), 4254–4284, doi:10.1080/01431161.2018.1452075, 2018.

770   Xu, H.: Modification of normalised difference water index (NDWI) to enhance open water features in remotely sensed imagery, Int. J. Remote Sens., 27(14), 3025–3033, doi:10.1080/01431160600589179, 2006.

Yang, J. and Huang, X.: The 30 m annual land cover dataset and its dynamics in China from 1990 to 2019, Earth Syst. Sci. Data, 13(8), 3907–3925, doi:10.5194/essd-13-3907-2021, 2021.

Yang, Q., Huang, X. and Tang, Q.: The footprint of urban heat island effect in 302 Chinese cities: Temporal trends and
775   associated factors, Sci. Total Environ., 655, 652–662, doi:10.1016/j.scitotenv.2018.11.171, 2019.

Zacharopoulou, D., Skopeliti, A. and Nakos, B.: Assessment and Visualization of OSM Consistency for European Cities, ISPRS Int. J. Geo-Information , 10(6), doi:10.3390/ijgi10060361, 2021.

Zha, Y., Gao, J. and Ni, S.: Use of normalized difference built-up index in automatically mapping urban areas from TM imagery, Int. J. Remote Sens., 24(3), 583–594, doi:10.1080/01431160304987, 2003.

780   Zhang, H. K., Roy, D. P., Yan, L., Li, Z., Huang, H., Vermote, E., Skakun, S. and Roger, J.-C.: Characterization of Sentinel-2A and Landsat-8 top of atmosphere, surface, and nadir BRDF adjusted reflectance and NDVI differences, Remote Sens. Environ., 215, 482–494, doi:https://doi.org/10.1016/j.rse.2018.04.031, 2018.

Zhang, X., Liu, L., Wu, C., Chen, X., Gao, Y., Xie, S. and Zhang, B.: Development of a global 30m impervious surface map using multisource and multitemporal remote sensing datasets with the Google Earth Engine platform, Earth Syst. Sci. Data,
785   12(3), 1625–1648, doi:10.5194/essd-12-1625-2020, 2020a.

Zhang, X., Liu, L., Chen, X., Gao, Y., Xie, S. and Mi, J.: GLC_FCS30: Global land-cover product with fine classification system at 30 m using time-series Landsat imagery, Earth Syst. Sci. Data Discuss., 1–31, doi:10.5194/essd-2020-182, 2020b.

Zhang, Y., Zhang, H. and Lin, H.: Improving the impervious surface estimation with combined use of optical and SAR remote sensing images, Remote Sens. Environ., 141, 155–167, doi:https://doi.org/10.1016/j.rse.2013.10.028, 2014.

790